

¹ **Broad-band ambient noise surface wave tomography
across the United States**

G. D. Bensen

³ Center for Imaging the Earth's Interior, Department of Physics, University
⁴ of Colorado at Boulder, Boulder, Colorado USA

M. H. Ritzwoller

⁵ Center for Imaging the Earth's Interior, Department of Physics, University
⁶ of Colorado at Boulder, Boulder, Colorado USA

N. M. Shapiro

⁷ Laboratoire de Sismologie, CNRS, IPGP, Paris, France

G. D. Bensen, Department of Physics, University of Colorado at Boulder, Campus Box 390,
Boulder, CO 80309, USA. (gbensen@colorado.edu)

Abstract.

This study presents surface wave dispersion maps across the contiguous United States determined using seismic ambient noise. Two years of ambient noise are used from March 2003 through February 2005 observed at nearly 200 broad-band seismic stations in the US, southern Canada, and northern Mexico. Cross-correlations are computed between all station-pairs to produce empirical Green functions. At most azimuths across the US, coherent Rayleigh wave signals exist in the empirical Green functions implying that ambient noise in the frequency band of this study (5 - 100 sec period) is sufficiently isotropically distributed in azimuth to yield largely unbiased dispersion measurements. Rayleigh and Love wave group and phase velocity curves are measured together with associated uncertainties determined from the temporal variability of the measurements. A sufficient number of measurements (>2000) is obtained between 8 sec and 25 sec for Love waves and 8 sec and 70 sec for Rayleigh waves to produce tomographic dispersion maps. Both phase and group velocity maps are presented in these period bands. Resolution is estimated to be better than 100 km across much of the US from 8-40 sec period for Rayleigh waves and 8-20 sec period for Love waves, which is unprecedented in a study at this spatial scale. At longer and shorter periods, resolution degrades as the number of coherent signals diminishes. The dispersion maps agree well with each other and with known geological and tectonic features and, in addition, provide new information about structures in the crust and uppermost mantle beneath much of the US.

1. Introduction

The purpose of this study is to produce surface wave dispersion maps across the contiguous United States using ambient noise tomography. We present Rayleigh and Love wave group and phase speed maps and assess their resolution and reliability. These maps display higher resolution and extend to shorter periods than previous surface wave maps that have been produced across the United States using traditional teleseismic surface wave tomography methods. The maps presented form the basis for an inversion to produce a higher resolution 3-D model of V_s in the crust and uppermost mantle, but this inversion is beyond the scope of the present paper.

Surface wave empirical Green functions (EGFs) can be determined from cross-correlations between long time sequences of ambient noise observed at different stations. In places we use the terms cross-correlogram and empirical Green function interchangeably, but they differ by an additive phase factor (e.g., *Lin et al.* [2007a]). Investigations of surface wave empirical Green functions have grown rapidly in the last several years. The feasibility of the method was first established by experimental (e.g., *Weaver and Lobbis* [2001], *Lobbis and Weaver* [2001], *Derode et al.* [2003], *Larose et al.* [2005]) and theoretical (e.g., *Snieder* [2004], *Wapenaar* [2004]) studies. *Shapiro and Campillo* [2004] demonstrated that the Rayleigh wave EGFs estimated from ambient noise possess dispersion characteristics similar to earthquake derived measurements and model predictions. The dispersion characteristics of surface wave empirical Green functions derived from ambient noise have been measured and inverted to produce dispersion tomography maps in several geographical settings, such as Southern California (*Shapiro et al.* [2005];

52 *Sabra et al.* [2005]), the western US (*Moschetti et al.* [2007]; *Lin et al.* [2007a]), Europe
53 (*Yang et al.* [2007]), Tibet (*Yao et al.* [2006]), New Zealand (*Lin et al.* [2007b]), Ko-
54 rea (*Cho et al.* [2007]), Spain (*Villasenor et al.* [2007]) and elsewhere. Most of these
55 studies focused on Rayleigh wave group speed measurements obtained at periods below
56 about 20 sec. *Campillo and Paul* [2003] showed that Love wave signals can emerge from
57 cross-correlations of seismic coda and *Gerstoft et al.* [2006] also noticed several signals
58 on transverse-transverse cross-correlations of ambient noise. These studies did not, how-
59 ever, demonstrate the consistent recovery of Love wave signals from ambient noise. *Lin*
60 *et al.* [2007a] placed both phase speed and Love wave measurements on a firm foundation
61 and showed that Love waves are readily observed using ambient noise. We follow their
62 methodology to present phase velocity and Love wave maps here in addition to group
63 velocity and Rayleigh wave maps. We apply ambient noise tomography on a geographical
64 scale much larger than all previous studies. The larger spatial scale also allows us to
65 extend the results to longer periods than in previous studies.

66 All of the results presented here are based on the data processing scheme described by
67 *Bensen et al.* [2007]. This method is designed to minimize the negative effects that result
68 from a number of phenomena, such as earthquakes, temporally localized incoherent noise
69 sources, and data irregularities. It also is designed to obtain dispersion measurements to
70 longer periods and along longer inter-station paths than in previous studies, and, thus,
71 increases the band-width and the geographical size of the study region.

72 Previous surface wave tomography across the North American continent was based on
73 teleseismic earthquake measurements. Several of these studies involved measurements
74 obtained exclusively across North America (e.g., *Alsina et al.* [1996], *Godey et al.* [2003],

75 *van der Lee and Nolet [1997]*) whereas others involved data obtained globally (e.g., *Tram-*
76 *pert and Woodhouse [1996]; Ekström et al. [1997]; Ritzwoller et al. [2002]*). Ambient noise
77 tomography possesses complementary strengths and weaknesses to traditional earthquake
78 tomography. Single-station earthquake tomography benefits from the very high signal-to-
79 noise ratio of teleseismic surface waves and the dispersion measurements extend to very
80 long periods (>100 sec) which results in constraints on deep upper mantle structures.
81 Several characteristics limit the power of traditional earthquake tomography, however.
82 First, teleseismic propagation paths make short period (< 20 sec) measurements difficult
83 to obtain in aseismic regions due to the scattering and attenuation that occur as distant
84 waves propagate. This is unfortunate because short period measurements are needed
85 to resolve crustal structures. This is particularly disadvantageous across the US, which
86 exhibits a low level of seismicity in most regions. Second, the long paths also result in
87 broad lateral sensitivity kernels which limits resolution to hundreds of kilometers. Third,
88 dispersion measurements from earthquakes typically have unknown uncertainties. Finally,
89 uncertainties in source location and depth manifest themselves in uncertainties in the “ini-
90 tial phase” of the measurement, which imparts an ambiguity to phase and group speeds
91 measured from earthquakes.

92 Although the empirical Green functions obtained by cross-correlating long time-series
93 between pairs of stations demonstrate a smaller signal-to-noise ratio than large earth-
94 quakes and the resulting ambient noise dispersion measurements typically are limited to
95 periods well below 100 sec, ambient noise tomography improves on each of the shortcom-
96 ings of traditional earthquake tomography. First, ambient noise empirical Green functions
97 provide dispersion maps to periods down to ~6 seconds (and lower in some places with

exceptionally dense station spacing), potentially with much better lateral resolution, particularly in the context of continental arrays of seismometers in which path density and azimuthal coverage can be very high. Second, one can estimate uncertainties from the repeatability of ambient noise measurements (e.g., *Bensen et al.* [2007]). Third, the station locations and the “initial phase” of the EGFs are both well known (*Lin et al.* [2007a]), so the measurements tend to be both more precise and more easily interpreted than earthquake signals.

Ambient noise tomography, therefore, provides a significant innovation in seismic methodology that is now yielding new information about the Earth with resolutions near the inter-station spacing. The currently developing Transportable Array component of EarthScope/USArray is being deployed on a rectangular grid and is now being used across the western US for ambient noise tomography by *Moschetti et al.* [2007]. Its traverse across the United States will not complete until the year 2014, however.

This paper is the first continental scale application of ambient noise tomography and is based on nearly 200 permanent and temporary stations throughout the contiguous US and in southern Canada and northern Mexico (Fig. 1a). Rayleigh wave tomography maps are created from 8 to 70 seconds period and Love wave maps from 8 to 25 sec. We present a subset of these maps. These maps provide new information about the crust and mantle beneath the United States, show that the technique is not limited to short periods or regional scales, and add further credibility to ambient noise surface wave tomography.

2. Data Processing

We follow the method described in detail by *Bensen et al.* [2007] for data processing from observations of ambient seismic noise to the production of group velocity measurements.

Phase speed measurements and Love wave data processing follow the procedure of *Lin et al.* [2007a]. We briefly review here the data processing procedure and discuss the repeatability of the dispersion measurements as well as the way in which signal-to-noise ratio (SNR) varies with period and region. In later sections, we discuss how measurements from almost 20,000 inter-station paths are selected to be used for tomographic inversion to estimate group and phase speed dispersion maps (*Barmin et al.* [2001]) ranging from 8 seconds to 70 seconds for Rayleigh waves and 8 to 25 seconds for Love waves. Only a subset of these maps, however, will be shown here.

We processed all available vertical and horizontal component broad-band seismic data from the 200 stations (Fig. 1a) that are available from the IRIS DMC and the Canadian National Seismic Network (CNSN) for the 24-month period from March 2003 through February 2005. Although the data come from this 24-month window, most time-series are shorter than 24-months because of station down time or installation during this period. Time-series lengths are referred to in terms of the time window from which the waveforms derived, but actual time-series lengths vary within the same time window. Station locations are identified in Figure 1a. Station coverage in the west and parts of the eastern mid-west is good, but the north-central US and the near-coastal eastern US are poorly covered. As seen later, this has ramifications for resolution. The azimuthal distribution of inter-station paths is shown in Figure 1b. This includes both inter-station azimuth and back-azimuth, presented as the number of paths falling into each 10° azimuth bin. Large numbers at a particular azimuth (or back-azimuth, both are included) correspond to the dominant inter-station directions. For example, in the eastern and central US, stations are oriented dominantly to pick up waves traveling to the north-east or the west. Concent-

trations of stations, such as in California, tend to produce large numbers of inter-station directions in a narrow azimuthal range. The diagrams are not azimuthally symmetric because azimuth and back-azimuth are not 180° -complements. Figure 1b dominantly reflects the geometry of the seismic network used. Later in the paper, we discuss the directions of propagation of the strongest signals and reference them to the azimuthal distribution of inter-station paths in Figure 1a.

Data preparation is needed prior to cross-correlation. Starting with instrument response corrected day-long time-series at each station, we first perform time-domain normalization to mitigate the effects of large amplitude events (e.g., earthquakes and instrument glitches). Initially, researchers favored a 1-bit (or sign bit, or binary) normalization (*Larose et al. [2004]*, *Shapiro et al. [2005]*), but *Bensen et al. [2007]* argued for the application of a temporally variable weighting function to retain more of the small amplitude character of the raw data and to allow for flexibility in defining the amplitude normalization in particular period bands. Here, we define the temporal normalization weights between periods of 15 and 50 sec, but apply the weights to the unfiltered data. As discussed by *Bensen et al. [2007]*, this removes earthquakes from the daily time-series more effectively than defining the temporal normalization on the raw data. The impact is seen most strongly in the quality of the Love wave signals. This procedure is applied to both the vertical and horizontal component data, but the relative amplitudes of the two horizontal components must be maintained. An additional spectral whitening is performed to all of the waveforms for each day to avoid significant spectral imbalance. Again, the same filter must be applied to both horizontal components. Spectral whitening increases the band-width of the automated broad-band dispersion measurements. (*Bensen et al. [2007]* present

¹⁶⁶ more details). After temporal and spectral normalization, cross-correlation is performed
¹⁶⁷ on day-long time-series for vertical-vertical, east-east, east-north, north-east, and north-
¹⁶⁸ north components. The horizontal components are then rotated to radial-radial (R-R)
¹⁶⁹ and transverse-transverse (T-T) orientations as defined by the great circle path between
¹⁷⁰ the two stations. These daily results are then “stacked” for the desired length of input
¹⁷¹ (e.g. one month, one year, etc.). The Rayleigh wave (Z-Z and R-R) and Love wave (T-T)
¹⁷² cross-correlograms yield two-sided (“causal” and “anticausal”) empirical Green functions
¹⁷³ corresponding to waves propagating in opposite directions between the stations. Both
¹⁷⁴ the causal and anticausal EGFs are equally valid and can be used as input into the dis-
¹⁷⁵ persión measurement routine, but may have different spectral content and signal-to-noise
¹⁷⁶ ratio characteristics. Both for simplicity and to optimize the band-width of the empirical
¹⁷⁷ Green functions, we average the causal and anticausal signals into a single “symmetric
¹⁷⁸ signal” from which all dispersion measurements are obtained.

¹⁷⁹ The frequency dependent group and phase velocities from the Rayleigh and Love wave
¹⁸⁰ EGFs are estimated using an automated dispersion measurement routine. Following *Lev-*
¹⁸¹ *shin et al.* [1972], we performed Frequency-Time Analysis (FTAN) to measure the phase
¹⁸² and group velocity dispersion on all recovered signals. The FTAN technique applies a
¹⁸³ sequence of Gaussian filters at a discrete set of periods and measures the group arrival
¹⁸⁴ times on the envelope of these filtered signals. Phase velocity is also measured and further
¹⁸⁵ details can be found in *Lin et al.* [2007a]. We used the 3D model of *Shapiro and Ritz-*
¹⁸⁶ *woller* [2002] to resolve the 2π phase ambiguity, which was successful in the vast majority
¹⁸⁷ of cases. The Rayleigh and Love wave signals apparent on the empirical Green functions
¹⁸⁸ are less complicated than earthquake signals because the inter-station path lengths are

relatively short and the absence of body waves simplifies the signal. This allowed the automation of the dispersion measurements. Selected examples of the symmetric component Rayleigh wave waveforms and the resulting group and phase speed measurements are shown in Figure 2a,b. The broad-band dispersive nature of these waveforms is seen in Figure 2a with longer period energy arriving first. Figure 2b shows the resulting group and phase dispersion curves. The fastest path lies between stations GOGA (Godfrey, GA, USA) and VLDQ (Val d'Or, Quebec, Canada) in the tectonically stable part of eastern North America. The slowest path is between stations DUG (Dugway, UT, USA) and ISA (Isabella, CA, USA) in the tectonically active part of the western US. The other two paths (Camsell Lake, NWT, Canada to Albuquerque, NM, USA; Cathedral Cave, MO, USA to Whiskeytown Dam, CA, USA) have intermediate speeds and propagate through a combination of tectonically deformed and stable regions.

Examination of the Rayleigh and Love wave signals reveals the difference between the speeds and signal strengths. Figure 3 presents examples of Z-Z, R-R, and T-T EGFs in the period range from 5 to 50 sec. Figure 3a contains the empirical Green functions between stations CCM (Crystal Cave, MO, USA) and RSSD (Black Hills, SD, USA) with an inter-station distance of 1226 km. Rayleigh waves are seen on the vertical-vertical (Z-Z) and radial-radial (R-R) cross-correlograms and arrive at similar times. Love wave signals are seen on the transverse-transverse (T-T) cross-correlograms. The different Rayleigh and Love wave arrival times are clear and are identified with different velocity windows in the diagram. Figure 3b,c present record sections for the Z-Z and T-T cross-correlograms from the 13 Global Seismic Network (GSN) stations (*Butler et al. [2004]*) in the study region.

²¹¹ Approximate move-outs of 3.0 and 3.3 km/sec for Rayleigh and Love waves are shown in
²¹² Figures 3b and 3c, respectively.

3. Data Selection

²¹³ After the empirical Green functions are computed between every station-pair for the
²¹⁴ Z-Z and T-T components, several selection criteria are applied prior to tomography. The
²¹⁵ effect of each step of the process in reducing the data set is indicated in Tables 1 and 2.

²¹⁶ First, we apply a minimum three wavelength inter-station distance constraint, which
²¹⁷ is imposed because of measurement instabilities at shorter distances and to be in accord
²¹⁸ with the far-field approximation (*Levshin et al.* [1999]; *Snieder* [2004]). This criterion
²¹⁹ significantly reduces the number of measurements at periods above 50 seconds because
²²⁰ stations must be separated by more than 600 km.

²²¹ Second, we apply a selection criterion based on the period-dependent signal-to-noise
²²² ratio (SNR), which is defined as the peak signal in a signal window divided by the root-
²²³ mean-square (RMS) of the trailing noise, filtered with a specified central period. Average
²²⁴ SNR values for the Z-Z, R-R, and T-T EGFs are seen in Figure 4. A dispersion mea-
²²⁵ surement is retained at a period only if the $\text{SNR} > 15$ for the cross-correlogram at that
²²⁶ period.

²²⁷ Similarities in the patterns of SNR as a function of period for Rayleigh waves on the
²²⁸ Z-Z and R-R components are observed in Figure 4 up to 20 seconds period; although
²²⁹ the R-R signal quality is lower. Above 20 sec, the R-R SNR degrades more quickly,
²³⁰ however, similar to the trend of the SNR for the T-T cross-correlations. This pattern is
²³¹ consistent with the results of *Lin et al.* [2007a]. Apparently, the SNR degrades at longer
²³² periods predominantly due to increasing levels of incoherent local noise, and may not be

due to decreasing signal levels. Because the SNR is much higher on the Z-Z than the R-R components and the Z-Z band-width is larger, we only use Rayleigh wave dispersion measurements obtained on the Z-Z cross-correlations.

Figure 5 presents information about the geographical distribution of signal quality. The average SNR of all waveforms is shown for Rayleigh (Z-Z) and Love (T-T) wave signals in each of the four regions defined in Figure 1a where both stations lie within the sub-region. SNR in the sub-regions is higher than over the entire data set (Fig. 4) because path lengths are shorter, on average, by more than a factor of two in the regional data. Rayleigh wave SNR is highest in the south-west region, with SNR in the other regions being lower but similar to each other. Long period SNR, in particular, is considerably higher in the south-west than in other regions. In most regions, the Rayleigh wave curves show double peaks apparently related to the primary and secondary microseism periods of 15 and 7.5 sec, respectively.

For Love waves, the highest SNR is in the south-west and north-west regions and the curves display only a single peak near the primary microseismic band, peaking in different regions between 13 and 16 sec period. The strongest Love waves are in the north-west, unlike the Rayleigh waves which are strongest in the south-west region. Thus, the distribution of Rayleigh and Love wave energies differ and they may not be co-generated everywhere. Although Figure 4 shows that below 15 sec period Love waves have a higher SNR than Rayleigh waves, this is true only in the western US. In the central and eastern US, Rayleigh and Love waves below about 15 sec have similar strengths. In all regions, Love wave signals are negligible above about 25 sec period. Love waves are much stronger in the western US than in the central or eastern US, particularly above about 15 sec

period. These results indicate clearly that the strongest ambient noise sources are located generally in westerly directions, although substantial Rayleigh wave signal levels also exist in the central and eastern US. Love waves in the central and eastern US, however, are much weaker above about 15 sec.

Third, we apply a data selection criterion based on the variability of measurements repeated on temporally segregated subsets of the data. We compiled cross-correlations for overlapping 6-month input time-series (e.g. June, July, August 2003 plus June, July, August 2004) to obtain 12 “seasonal” stacks. We measure the dispersion curves on data from each 6-month (dual 3-month) time window and on the complete 24-month time window. For each station-pair, the standard deviation of the dispersion measurements is computed at a particular period using data from all of the 6-month time windows in which $\text{SNR} > 10$ at that period. An illustration of this procedure appears in Figure 6. Figure 6a shows the Z-Z, R-R, and T-T EGFs used from the 2685 km path between stations DWPF (Disney Wilderness Preserve, FL, USA) and RSSD (Black Hills, SD, USA). Figure 6b,c,d compares the measurements obtained on the 6-month temporal subsets of data with the 24-month group and phase velocity measurements. The error bars indicate the computed standard deviation. If fewer than four 6-month time-series satisfy the criterion that $\text{SNR} > 10$, then the standard deviation of the measurement is considered indeterminate and we assign three times the average of the standard deviations taken over all measurements within the data set. The average standard deviation values are shown in Figure 7. Finally, we reject measurements for a particular wave type (Rayleigh/Love, group/phase speed) and period if the estimated standard deviation is greater than 100 meters/sec, as this

278 indicates an instability in the measurement. The inverse of the standard deviation is used
279 as a weight in the tomographic inversion (e.g., *Barmin et al.* [2001]).

280 In contrast with Figure 7, Figure 8 contains the mean measurement standard deviation
281 values for each of the four sub-regions defined in Figure 1a. The measurements are labeled
282 for Rayleigh and Love wave group and phase measurements. The patterns are similar
283 for all sub-regions. Because dramatic differences between measurement uncertainties in
284 different regions are not observed, similar measurement quality is obtained in all regions
285 even though there are differences between the regions in average SNR and, therefore,
286 different numbers of measurements in each region. The most stable measurements are
287 Rayleigh wave phase speeds, particularly above about 20 sec where phase speed is more
288 robust than group speed. Below 20 sec period, the envelope on which group velocity is
289 measured becomes narrower at short periods and increases measurement precision. Thus,
290 the accuracy of the group velocity measurements becomes similar to the phase velocity
291 measurements below 20 sec period. Although the Love wave phase velocity measurements
292 have favorable standard deviation with increasing period, the number of high quality
293 measurements above 20 sec period drops precipitously due to low signal levels. Finally, as
294 a rule-of-thumb, at periods above about 30 sec, the standard deviation of Rayleigh wave
295 phase speed measurements is about half that of group speed.

296 Fourth, we apply a final data selection criterion based on tomographic residuals. Using
297 the thus far accepted measurements, we create an overly-smoothed tomographic dispersion
298 map for each wave type (Rayleigh/Love, group/phase velocity). Measurements for each
299 wave type with high travel time residuals (three times the root-mean-squared residual
300 value at a given period and wave type) are removed and the overly smoothed disper-

301 sion map is recreated, becoming the background dispersion map for the later finer-scale
302 inversion.

303 The final Rayleigh wave (Z-Z) path retention statistics for selected periods are shown
304 in Table 1. Similar statistics for Love waves (T-T) at periods of 10, 16 and 25 seconds
305 period are shown in Table 2. The number of paths retained at periods above about 70 sec
306 for Rayleigh waves and 25 sec for Love waves is insufficient for tomography across the US,
307 but the longer period measurements are useful in combination with teleseismic dispersion
308 measurements.

4. Azimuthal distribution of signals

309 The theoretical basis for surface wave dispersion measurements obtained on ambient
310 noise and the subsequent tomography assumes that ambient noise is distributed homo-
311 geneously with azimuth (e.g., *Snieder* [2004]). Asymmetric two-sided cross-correlograms,
312 such as those in Figure 3a and documented copiously elsewhere (e.g., *Stehly et al.* [2006]),
313 illustrate that the strength and frequency content of ambient noise varies appreciably
314 with azimuth. This motivates the question as to whether ambient noise is well enough
315 distributed in azimuth to return unbiased dispersion measurements for use in tomogra-
316 phy. *Lin et al.* [2007a] present evidence, based on measurements of the “initial phase” of
317 phase speed measurements from a three-station method, that in the frequency band they
318 consider (6 - 40 seconds period) ambient noise is distributed sufficiently isotropically so
319 that phase velocity measurements are returned largely unbiased. Another line of evidence
320 that supports the robustness of the dispersion measurements derived from ambient noise
321 comes from the variability of the dispersion measurements, as the directional content of
322 ambient noise varies between seasons. This is, of course, the basis for our error analysis.

323 Here, we take another approach, and attempt to map the direction of propagation of rel-
324 atively large amplitude signals. We are not interested exclusively in the directions from
325 which the largest amplitude signals emanate, which have interested researchers who aim
326 to understand the strongest sources of ambient noise (e.g., *Stehly et al.* [2006]). Rather,
327 we are interested in the directions of propagation of all coherent signals that rise above
328 background incoherent noise because these signals form the basis for the ambient noise
329 tomographic method. In this assessment, the distribution of paths dictated by the geom-
330 etry of the array must be borne in mind. Consequently, all results are taken relative to
331 the azimuthal distributions presented in Figure 1b.

332 Figure 9 presents the azimuthal distribution of large amplitude Rayleigh wave signals
333 at periods of 8, 14, 25 and 40 sec. Our measurements are divided into three sub-regions as
334 defined in Figure 1a, but with the central and eastern regions combined. Only one station
335 in each station-pair is required to be in a sub-region. Both azimuth and back-azimuth are
336 included in the figure. Averaging over all regions and azimuths, at periods of 8, 14, 25,
337 and 40 sec the fraction of Rayleigh wave EGFs with a SNR > 10 is 0.38, 0.49, 0.54 and
338 0.38, respectively, and reduces quickly for periods above 40 sec. To compute this fraction
339 as a function of azimuth, the number of paths with SNR > 10 in a given 20° azimuth bin
340 is divided by the total number of paths in that bin given by Figure 1b. The SNR on both
341 cross-correlation lags is considered separately, and the indicated azimuth is the direction
342 of propagation. We refer to the positive and negative lag contributions as having come
343 from different “paths” for simplicity, but, in fact, the paths are the same and only the
344 azimuths differ.

345 Inspection of Figure 9 reveals that the fraction of relatively high SNR paths at a given
346 azimuth is fairly homogeneously distributed with azimuth. At 14 sec and 25 sec period,
347 in all three regions all azimuths have the fraction of paths with SNR >10 above 20% and,
348 hence, the distribution of useful ambient noise signals is fairly homogeneous, even though
349 the highest SNR signals may arrive from only a few principal directions. At 8 seconds
350 period, the results are not as geographically consistent. In the two western regions, the
351 strongest signals are those with noise coming from the west. This agrees with the notion
352 that these results would be dominated by the 7.5 sec period secondary microseism. In
353 the east and central regions, however, signals come both from the west and northeast and
354 there are fewer high SNR cross-correlations. Finally, moving to 40 sec period, the overall
355 fraction of high SNR measurements is lower. Relative to this lower level, the azimuthal
356 distribution again has a homogeneous component although certain azimuths have a higher
357 fraction of high SNR paths. The azimuthal pattern above 40 sec in each region remains
358 about the same as at 40 sec, but the fraction of high SNR observations diminishes rapidly.

359 Similar results are obtained for Love waves, as can be seen in Figure 10. Strong Love
360 wave signals are most isotropic in the primary microseismic band, the center column in
361 Figure 10. In the secondary microseismic band, strong Love waves are less isotropic, par-
362 ticularly in the Central US. Nevertheless, azimuthal coverage fairly homogeneous. Above
363 20 sec period, period, however, the number of large amplitude signals diminishes rapidly,
364 particularly in the east. In the west, some large amplitude signals exist, but emerge
365 dominantly from the northwest and southeast directions. Both signal amplitude and az-
366 imuthal distribution above 20 sec period, therefore, are insufficient for tomography on a
367 large scale.

³⁶⁸ In conclusion, therefore, at all periods, in all regions and most azimuths, coherent
³⁶⁹ Rayleigh wave signals exist in ambient noise. This is least true at periods below 10 sec,
³⁷⁰ where most of the Rayleigh wave energy is coming generally from the west, but even
³⁷¹ in this case the well sampled azimuths cover nearly 180 degrees. Coherent Love wave
³⁷² signals exist at most azimuths from 8 sec to 20 sec period, but at longer periods both the
³⁷³ azimuthal coverage and the strength of Love waves diminish rapidly. These observations
³⁷⁴ provide another item in a growing list of evidence indicating that ambient noise in this
³⁷⁵ frequency band is sufficiently isotropically distributed in azimuth to yield largely unbiased
³⁷⁶ dispersion measurements.

5. Tomography

³⁷⁷ An extensive discussion of the tomography procedure is presented in *Barmin et al.*
³⁷⁸ [2001]. We follow their discussion to provide a basic introduction to the overall procedure
³⁷⁹ and define some needed terms. The tomographic inversion is a 2-D ray theoretical method,
³⁸⁰ similar to a Gaussian beam technique and assumes wave propagation along a great circle
³⁸¹ but with “fat” rays. Starting with observed travel times we estimate a model \mathbf{m} (2-D
³⁸² distribution of surface wave slowness) by minimizing the penalty functional:

$$(\mathbf{G}(\mathbf{m}) - \mathbf{d})^T \mathbf{C}^{-1} (\mathbf{G}(\mathbf{m}) - \mathbf{d}) + \alpha^2 \| F(\mathbf{m}) \|^2 + \beta^2 \| H(\mathbf{m}) \|^2, \quad (1)$$

³⁸³ where \mathbf{G} is the forward operator computing travel times from a model, \mathbf{d} is the data matrix
³⁸⁴ of measured surface wave travel times, and \mathbf{C} is the data covariance matrix assumed here
³⁸⁵ to be diagonal and composed of the square of the measurement standard deviations. $F(\mathbf{m})$

³⁸⁷ is the spatial smoothing function where

$$\text{388} \quad F(\mathbf{m}) = m(\mathbf{r}) - \int_S S(\mathbf{r}, \mathbf{r}') m(\mathbf{r}') d\mathbf{r}', \quad (2)$$

³⁸⁹ and

$$\text{390} \quad S(\mathbf{r}, \mathbf{r}') = K_0 \exp\left(-\frac{|\mathbf{r} - \mathbf{r}'|^2}{2\sigma^2}\right) \quad (3)$$

³⁹¹ where

$$\text{392} \quad \int_S S(\mathbf{r}, \mathbf{r}') d\mathbf{r}' = 1, \quad (4)$$

³⁹³ and \mathbf{r} is the target location and \mathbf{r}' is an arbitrary location. The function H penalizes the
³⁹⁴ model in regions with poor path or azimuthal coverage. The contributions of H and F
³⁹⁵ are controlled by the damping parameters α and β while spatial smoothing (related to
³⁹⁶ the fatness of the rays) is controlled by adjusting σ . These three parameters (α , β and
³⁹⁷ σ) are user controlled variables that are determined through trial and error optimization.

³⁹⁸ The resulting spatial resolution is found at each point by fitting a 2-D Gaussian function
³⁹⁹ to the resolution matrix (map) defined as follows:

$$\text{400} \quad A \exp\left(-\frac{|\mathbf{r}|^2}{2\gamma^2}\right) \quad (5)$$

⁴⁰¹ where \mathbf{r} here denotes the distance from the target point. The standard deviation of the
⁴⁰² Gaussian function, γ , is useful for understanding the spatial size of the features that can be
⁴⁰³ determined reliably in the tomographic maps. In this paper, we report 2γ as the resolution,
⁴⁰⁴ the full-width of the resolution kernel at each point. Figure 11a shows the resolution map
⁴⁰⁵ for the 10 sec Rayleigh wave group speed. The corresponding ray coverage is shown in
⁴⁰⁶ Figure 11b. The more densely instrumented regions, such as southern California and near
⁴⁰⁷ the New Madrid shear zone in the central United States, have resolution < 70 km, which

is better than the inter-station spacing in these regions. Across most of the US, resolution averages about 100 km for Rayleigh waves up to 40 sec and then degrades to 200 km at 70 sec period. For Love waves, resolution averages about 130 km below 20 sec, but then rapidly degrades at longer periods so that at 20 sec the average resolution is about 200 km. The rapid degradation of average resolution in the US for Love waves is due to the loss of Love wave signals in the eastern US, which sets on at about 15 sec, as discussed above. Regions with resolution worse than 1000 km are indicated on the tomographic maps in grey and, in addition, to outline the high resolution regions we plot the 200 km resolution contours.

We use ray theory as the basis for tomography in this study, albeit with “fat rays” given by the correlation length parameter σ . In recent years, surface wave studies have increasingly moved toward diffraction tomography using spatially extended finite-frequency sensitivity kernels based on the Born/Rytov approximation (*Spetzler et al. [2002]; Ritzwoller et al. [2002]; Yoshizawa and Kennett [2002]*; and many others). *Ritzwoller et al. [2002]* showed that ray theory with fat rays produces similar structure to diffraction tomography in continental regions at periods below 50 seconds and the similarities strengthen as path lengths decrease. *Yoshizawa and Kennett [2002]* argued that the spatial extent of sensitivity kernels is effectively much less than given by the Born/Rytov theory, being confined to a relatively narrow “zone of influence” near the classical ray. They conclude, therefore, that in many applications, off-great-circle propagation may provide a more important deviation from straight-ray theory than finite frequency effects. *Ritzwoller and Levshin [1998]* show that off-great-circle propagation can be largely ignored at periods above about 30 seconds for paths with distances less than 5000 km, except in extreme

cases. From a practical perspective then, these arguments support the contention that ray-theory with ad-hoc fat rays can adequately represent wave propagation for most of the path lengths and most of the period range under consideration here. A caveat is for relatively long paths (> 1000 km) at short periods (< 20 sec), in which case off-great-circle effects may become important. Off-great-circle effects will be largest near structural gradients, but are mitigated by observations made on orthogonal paths. In our study region, where structural gradients are largest azimuthal path coverage tends to be quite good. These considerations lead us to believe that ray theory with fat-rays is sufficient to produce meaningful dispersion maps and that uncertainties in the maps produced by the arbitrariness of the choice of the damping parameters are probably larger than errors induced by the simplified theory. Nevertheless, future work is called for to test this assertion and to quantify how fully modeling off great-circle propagation would change the maps. We anticipate only subtle changes.

6. Results

In this section we present examples of the tomographic maps with the particular purpose of establishing their credibility and limitations. In the next section, we qualitatively discuss some of the structural features that appear in the maps.

This tomography method is applied to the final set of accepted measurements to produce dispersion maps from 8 to 70 sec period for Rayleigh waves and 8 to 25 sec period for Love waves. In this period range more than 2000 measurements exist for all wave types. The method is applied on a $0.5^\circ \times 0.5^\circ$ geographical grid across the study region. Examples of the resulting dispersion maps are presented in Figures 12 - 15. In all maps, the 200 km resolution contour is shown with a thick black or grey contour and the grey regions are

453 those areas on the continent that have indeterminate velocities. The damping parameters
454 α and β in equation (1) which control the strength of the smoothness constraint and the
455 tendency of the inversion to stay at the input model are determined subjectively to supply
456 acceptable fit to the data, while retaining the coherence of large-scale structures and
457 controlling the tendency of streaks and stripes to contaminate the maps. The smoothing
458 or correlation length parameter, σ , is chosen to be 125 km at periods below 25 sec and
459 150 km at longer periods. As with any tomographic inversion, the resulting maps are not
460 unique but the features that we discuss below are common to any reasonable choice of
461 the damping and smoothness parameters.

462 Discussion of the tomographic maps is guided by the vertical V_s sensitivity kernels
463 shown in Figure 16. At a given period, phase velocity measurements tend to sense deeper
464 structures than group velocity measurements and Rayleigh waves sense deeper than Love
465 waves. Thus, at any period the Rayleigh wave phase velocities will have the deepest
466 sensitivity and the Love wave group velocities will be most sensitive to shallow structures.

467 Figures 12 and 13 show Rayleigh and Love wave group and phase speed maps at 10 and
468 20 sec period, respectively. Sedimentary thickness contours are over-plotted in Figure 12
469 and will be discussed further in the next section. The 10 sec maps are all similar to one
470 another, with much lower speeds in the western than the eastern US. The similarity of
471 the maps is expected because these wave types are all predominantly sensitive to crustal
472 structures, notably the existence of sediments. Thus, the principal features on these maps
473 are slow anomalies correlated with sedimentary basins, as discussed later. The 20 sec
474 maps are also similar to one another, with the exception of the Rayleigh phase velocity
475 map. The 20 sec Rayleigh group velocity and Love wave group and phase velocity maps

476 are more similar to the 10 sec maps than the 20 sec phase velocity map. This is because,
477 like the 10 sec results, these maps are mostly sensitive to the wave speeds within the
478 crust. This similarity between these maps lends credence to the tomographic results at
479 short periods.

480 As Figure 16b shows, the 20 sec Rayleigh wave phase velocity map has a substantial sen-
481 sitivity to the mantle and is better correlated with intermediate period maps. Examples
482 of results at intermediate periods are shown in Figure 14, which presents a comparison
483 between the 25 sec Rayleigh wave phase speed and the 40 sec Rayleigh wave group speed
484 maps. Figure 16c also shows that these two wave types have very similar vertical sensitiv-
485 ity kernels, both waves being predominantly sensitive to shear velocities in the uppermost
486 mantle. The measurements, however, are entirely different. We view the similarity be-
487 tween these maps, therefore, as a confirmation of the procedure at intermediate periods.

488 The longest period map presented here is the 60 sec Rayleigh wave phase speed map
489 shown in Figure 15a. This map possesses considerable sensitivity to the upper mantle to a
490 depth of about 150 km. It is compared to the map for the same wave type computed from
491 the 3-D model of *Shapiro and Ritzwoller* [2002] shown in Figure 15b. At large scales, the
492 maps are similar both in the distribution and absolute value of velocity. A more damped
493 version of the ambient noise result agrees even better with the model prediction. The 3-D
494 model is radially anisotropic, and the agreement of absolute levels indicates that the model
495 appears to account for anisotropy accurately. The transition between the low velocities of
496 the tectonically active western US and the stable eastern US craton are largely consistent
497 between the 3-D model and the ambient noise result. There are a few discrepancies,
498 however, particularly in Texas where the ambient noise indicates mostly low velocities

499 but with high velocities in the western Texas pan-handle. The lowest velocities in both
500 maps lie in northern Nevada and southern Oregon. Of course, smaller scale anomalies
501 appear in the ambient noise map. In particular, very low velocity anomalies appear in the
502 Salton Trough in southern California and west of the Rio Grande Rift in New Mexico.
503 High velocities extend into the southeastern US, particularly in Alabama.

504 The fit of individual dispersion measurements to the tomographic maps reveals more
505 about the quality of the data. The first type of information is the variance reduction rela-
506 tive to a homogeneous model, which here is taken to be the average of the measurements
507 at each wave type and period. Figure 17a shows the variance reduction for the Rayleigh
508 and Love wave group and phase speed maps from 10 to 90 sec period. (Rayleigh wave
509 maps above 70 sec and Love wave maps above 25 sec are created in order to extend these
510 statistics to the longer periods.) The largest variance reductions are for the Rayleigh wave
511 phase velocity measurements, which are above 90% for the entire period range. Below
512 20 sec period, a similar variance reduction is achieved by the Rayleigh wave group speed
513 maps. Love wave variance reduction is mostly lower. Love wave results above about 25
514 sec period are of little meaning because the number of measurements is so low. For all
515 wave types, the mean path length stays nearly the same (around 1800 km) for all periods.
516 The variance reduction reflects the residual level after tomography, which is plotted both
517 in time and velocity in Figure 17b,c. Rayleigh wave phase velocity residuals are between 2
518 and 3 sec across the whole band, and time residuals for the other waves are mostly between
519 6 and 10 sec. In particular, Rayleigh wave group velocity residuals are 2-3 times larger
520 than the anomalies for Rayleigh phase velocity, consistent with the standard deviation of
521 the phase velocity measurement being about half that for group velocity.

7. Discussion

522 Detailed interpretation of surface wave dispersion maps is difficult because their sensi-
523 tivity kernels are extended in depth and for group velocities they actually change sign.
524 We present a qualitative discussion of Figures 12 - 15 here, but a more rigorous interpre-
525 tation must await a 3-D inversion, which is beyond the scope of this paper. Many of the
526 features of the maps in Figures 12 - 15 are not surprising, as they represent structures on
527 a larger spatial scale similar to those revealed by the earlier work of *Shapiro et al.* [2005],
528 *Lin et al.* [2007b], and *Moschetti et al.* [2007] in the western US. The details of the maps
529 and how they vary with period, particularly at longer period parts and in the eastern US,
530 are entirely new, however.

531 Overall, the most prominent anomaly on all maps is the continental-scale east-west
532 dichotomy between the tectonically active western US and the cratonic eastern US. This
533 dichotomy is observed at all periods, so it expresses both crustal and mantle structures,
534 although its contribution tends to grow with increasing period, at least in a relative
535 sense. In terms of smaller scale regional structures, lateral crustal velocity anomalies
536 that manifest themselves in surface wave dispersion maps are largely compositional in
537 origin, whereas the mantle anomalies are predominantly thermal, although volatile content
538 may also contribute to low velocity anomalies in both the crust and mantle. The most
539 significant shallow crustal lateral velocity anomalies are due to velocity differences between
540 the sedimentary basins and surrounding crystalline rocks, which are more significant than
541 velocity variations within the crystalline crust. Large-scale anomalies in the uppermost
542 mantle correspond to variations in lithospheric structure and thickness, predominantly
543 reflecting differences between the tectonic lithosphere of the western US and cratonic

544 lithosphere of the eastern and central US. Regional scale anomalies reflect variations in
545 the thermal state of the uppermost mantle and crustal thickness.

546 Below 20 sec period (i.e., Figures 12 and 13), the dispersion maps dominantly reflect
547 low velocity anomalies caused by sedimentary basins. The sediment model of (*Laske and*
548 *Masters [1997]*) is shown in Figure 18 for comparison, with several principal structural
549 units identified. Isopach contours are superimposed in Figure 12 with a 1 km interval for
550 reference. The 10 sec period maps reveal low velocity anomalies associated with sediments
551 in the Great Valley (CV) of central California as well as the Salton Trough/Imperial Val-
552 ley of southern California extending down into the Gulf of California (GC). Low velocity
553 anomalies are also coincident with the Anadarko (AB) basin in Texas/Oklahoma and the
554 Permian Basin (PB) in west Texas. The deep sediments in the Gulf of Mexico (GOM)
555 produce the largest low velocity features. Other basins such as the Wyoming-Utah-Idaho
556 thrust belt (TB) extending north to the Williston basin (WB) also are apparent. This fea-
557 ture is seen best on the Love wave group speed map (Figure 12c) which has the shallowest
558 sensitivity (see Figure 16a). Rayleigh wave phase speed on the other hand has deeper
559 sensitivity and the Williston basin is only vaguely seen as a relative low velocity feature
560 in Figure 12b. The Appalachian Basin (ApB) also appears as a relative slow anomaly
561 in all the maps, although it is less pronounced due to the generally higher wave speeds
562 and older (hence faster) sediments in the eastern US. The Michigan Basin (MB) is not
563 observed, probably because of the lower resolution in the central US than in west where
564 station coverage is better.

565 Low wave speeds observed in the 10 sec maps for the Basin and Range (BR) or Pacific
566 Northwest (PNW) are interesting considering the lack of deep sedimentary basins. These

567 anomalies, therefore, are probably due to thermal or compositional anomalies within the
568 crystalline crust rather than in the sediment overburden.

569 Many of the features of the 10 sec maps in Figure 12 are also seen in the 20 sec maps of
570 Figure 13. The range of depth sensitivities for the 20 sec dispersion maps is broad (Figure
571 16), however, and the Rayleigh wave phase speed map (Figure 13b) is more like other
572 intermediate period maps. In addition, the shallower and older basins are not observed
573 and the Sierra Nevada (SN) high velocity anomaly emerges more clearly at 20 sec than
574 at 10 sec period. High speed anomalies are observed in the Gulf of California, in contrast
575 to the 10 sec maps, due to thin oceanic crust.

576 At intermediate periods (25 - 40 sec), waves are primarily sensitive to depths between
577 25 and 70 km; namely, the deep crust (in places), crustal thickness, and the uppermost
578 mantle. The Rayleigh wave 25 sec phase speed map and the 40 sec group speed map
579 have maximum sensitivities at about 50 km depth and similar kernels, as Figure 16 il-
580 lustrates. Thick crust will tend to appear as slow velocity anomalies and thin crust as
581 fast anomalies, for example. The anomalies on the maps in Figure 14 are similar to one
582 another, with a few exceptions. The low velocity anomalies through the Rocky Mountain
583 Region (RM, Colorado, Wyoming, eastern Utah, southern Idaho) and the Appalachian
584 Mountains (ApM, northern Alabama to western Pennsylvania) are probably the most
585 prominent low velocity features and they reflect thicker crust than average. To focus on
586 this further, the box identified in the western panel of Figure 14b is shown in greater de-
587 tail in Figure 19. Over-plotted in this figure is the depth to Cornell Moho model (see
588 http://discoverourearth.org/geoid/metadata/htmls/image_grid/us_moho_eq.html)
589 with a 2.5 km contour interval. In general, areas with thicker crust in Nevada, Utah,

590 Idaho, Wyoming, and Colorado have slower wave speeds, as expected. The bone-shaped
591 high velocity anomaly of eastern Nevada corresponds to thinner crust beneath the Great
592 Basin. East of Colorado, however, crustal velocities are higher due to the east-west tec-
593 tonic dichotomy of the US and the lithosphere thickens beneath cratonic North America,
594 which partially compensate for the low velocities that result from the thick crust. For
595 this reason, the low velocities beneath the Rocky Mountain region do not extend into the
596 central US. Nevertheless, the low velocities of the Colorado Plateau probably also reflect
597 elevated crustal temperatures in addition to thicker crust. High velocity anomalies along
598 the coasts, in southern Arizona, and northwestern Mexico reflect thinner crust in these
599 regions.

600 Not all low velocity anomalies at intermediate periods have their origin in thicker crust.
601 In the Pacific Northwest (PNW) states of northern California, Oregon, and Washington,
602 slow anomalies are probably caused by a warm, volatilized mantle wedge overlying the
603 subducting Juan de Fuca Plate. These low velocities are not seen south of the Mendocino
604 triple junction where the Farallon slab is no longer present in the shallow mantle. Perhaps
605 surprisingly, the effect of the Anadarko Basin (AB) in western Oklahoma persists to these
606 periods. Figure 16c illustrates that at intermediate periods very shallow structures will
607 have a contribution to surface wave speeds.

608 Some features differ between the 25 sec group speed and the 40 sec phase speed maps,
609 however. We note two. First, the 40 sec phase speed map has low velocities extending
610 east into Nebraska and South Dakota, whereas these features are more subdued on the 25
611 sec group speed map. Second, the 25 sec group speed map has a high velocity anomaly
612 in Michigan which is largely missing on the 40 sec phase speed map, although Michigan

613 does appear as a relatively fast feature in this map. These discrepancies are small, and
614 overall the maps agree quite well.

615 Moving to mantle sensitivity, Figure 15a shows the phase speed map at 60 sec period.
616 This wave is most sensitive to depths from 50 to 150 km and reveals features of mantle
617 structure and lithospheric thickness, in contrast to the shallower sensitivity of maps in
618 Figure 14. The cold, thick lithosphere beneath the cratonic core of the continent appears
619 clearly as a fast anomaly in the central and eastern US, while the thinner lithosphere in the
620 western United States appears as low velocities over a large area. The transition between
621 the tectonic and cratonic lithosphere is similar in both maps, although the ambient noise
622 map has low velocities pushing further to the east in Colorado. In addition, the expression
623 of the Anadarko Basin is still seen at this period in western Oklahoma and the Texas
624 Panhandle. The lowest velocities of the map are in the high lava plains of southeast
625 Oregon and northwest Nevada, which is believed to be the location of the first surface
626 expression of the plume that currently underlies Yellowstone. Yellowstone itself is below
627 the resolution of the maps presented in this study. However, a low velocity anomaly does
628 appear in the maps based on the Transportable Array component of EarthScope/USArray
629 (*Moschetti et al. [2007]; Lin et al. [2007b]*). Very low velocities are also associated with
630 the Sierra Madre Occidental in western Mexico, which is a Cenozoic volcanic arc.

8. Conclusions

631 We computed cross-correlations of long time sequences of ambient seismic noise to
632 produce Rayleigh and Love wave empirical Green functions between pairs of stations across
633 North America. This is the largest spatial scale at which ambient noise tomography has
634 been applied, to date. Cross-correlations were computed using up to two years of ambient

noise data recorded from March of 2003 to February of 2005 at ~200 permanent and temporary stations across the US, southern Canada, and northern Mexico. The period range of this study is from about 5 sec to 100 sec. We show that at all periods and most azimuths across the US, coherent Rayleigh wave signals exist in ambient noise. Thus, ambient noise in this frequency band across the US is sufficiently isotropically distributed in azimuth to yield largely unbiased dispersion measurements.

Rayleigh and Love wave group and phase speed curves were obtained for every inter-station path, and uncertainty estimates (standard deviations) were determined from the variability of temporal subsets of the measurements. Phase velocity standard deviations are about half the group velocity standard deviations, on average. These uncertainty estimates and the frequency dependent signal-to-noise ratios were used to identify the robust dispersion curves, with total numbers changing with period and wave type up to a maximum of about 9000. Sufficient numbers of measurements (more than 2000) to perform surface wave tomography were obtained for Love waves between about 8 sec and 25 sec period and for Rayleigh waves between about 8 sec and 70 sec period. A subset of these maps are presented herein. Resolution (defined as twice the standard deviation of a 2-D Gaussian function fit to the resolution surface at each point) is estimated to be better than 100 km across much of the US at most periods, but it degrades at the longer periods and degenerates sharply near the edges of the US, particularly near coastlines. This resolution is unprecedented in a study at the spatial scale of this one.

In general, the dispersion maps agree well with each other and with known geological features and, in addition, provide new information about structures in the crust and uppermost mantle beneath much of the US. Inversion to estimate 3-D structure in the

658 crust and uppermost mantle and to constrain crustal anisotropy are natural extensions of
659 this work.

660 **Acknowledgments.** All of the data used in this research were downloaded either from
661 the IRIS Data Management Center or the Canadian National Data Center (CNDC). This
662 research was supported by a contract from the US Department of Energy, DE-FC52-
663 2005NA26607, and two grants from the US National Science Foundation, EAR-0450082
664 and EAR-0408228 (GEON project support for Bensen).

References

- 665 Alsina, D., R. L. Woodward, and R. K. Snieder (1996), Shear wave velocity structure in
666 North America from large-scale waveform inversions of surface waves, *J. Geophys. Res.*,
667 101(B7), 15,969–15,986.
- 668 Barmin, M., M. Ritzwoller, and A. Levshin (2001), A fast and reliable method for surface
669 wave tomography, *Pure Appl. Geophys.*, 158(8), 1351–1375.
- 670 Bensen, G. D., M. H. Ritzwoller, M. P. Barmin, A. L. Levshin, F. Lin, M. P. Moschetti,
671 N. M. Shapiro, and Y. Yang (2007), Processing seismic ambient noise data to obtain
672 reliable broad-band surface wave dispersion measurements, *Geophys. J. Int.*, (169),
673 1239–1260.
- 674 Butler, R., et al. (2004), The Global Seismographic Network surpasses its design goal,
675 *EOS Trans. AGU*, 85(23), 225–229.
- 676 Campillo, M., and A. Paul (2003), Long-range correlations in the diffuse seismic coda,
677 *Science*, 299(5606), 547–549.

- 678 Cho, K., R. Herrmann, C. Ammon, and K. Lee (2007), Imaging the upper crust of the
679 Korean Peninsula by surface-wave tomography, *Bull. Seis. Soc. Am.*, 97(1B), 198–207.
- 680 Derode, A., E. Larose, M. Campillo, and M. Fink (2003), How to estimate the Green's
681 function of a heterogeneous medium between two passive sensors? Application to acous-
682 tic waves, *Appl. Phys. Lett.*, 83(15), 3054–3056.
- 683 Ekström, G., J. Tromp, and E. Larson (1997), Measurements and global models of surface
684 wave propagation, *J. Geophys. Res.*, 102, 8137–8157.
- 685 Gerstoft, P., K. Sabra, P. Roux, W. Kuperman, and M. Fehler (2006), Greens functions
686 extraction and surface-wave tomography from microseisms in southern California, *Geo-
687 physics*, 71(4), 123–131.
- 688 Godey, S., R. Snieder, A. Villaseñor, and H. M. Benz (2003), Surface wave tomography
689 of North America and the Caribbean using global and regional broad-band networks:
690 phase velocity maps and limitations of ray theory, *Geophys. J. Int.*, 152(3), 620–632.
- 691 Larose, E., A. Derode, M. Campillo, and M. Fink (2004), Imaging from one-bit correlations
692 of wideband diffuse wave fields, *J. Appl. Phys.*, 95(12), 8393–8399.
- 693 Larose, E., A. Derode, D. Clorennec, L. Margerin, and M. Campillo (2005), Passive
694 retrieval of Rayleigh waves in disordered elastic media, *Phys. Rev. E*, 72(4), 46,607–
695 46,607.
- 696 Laske, G., and G. Masters (1997), A global digital map of sediment thickness, *EOS Trans.
697 AGU*, 78, 483.
- 698 Levshin, A., V. Pisarenko, and G. Pogrebinsky (1972), On a frequency-time analysis of
699 oscillations, *Ann. Geophys.*, 28(2), 211–218.

- 700 Levshin, A., M. Ritzwoller, and J. Resovsky (1999), Source effects on surface wave group
701 travel times and group velocity maps, *Phys. Earth Planet. Int.*, 115, 293–312.
- 702 Lin, F., M. P. Moschetti, and M. H. Ritzwoller (2007a), Phase-velocity measurement of
703 Rayleigh wave based on ambient noise seismology, *Geophys. J. Int.*, in preparation.
- 704 Lin, F., M. H. Ritzwoller, J. Townend, M. Savage, and S. Bannister (2007b), Ambient
705 noise Rayleigh wave tomography of New Zealand, *Geophys. J. Int.*, doi:10.1111/j.1365-
706 246X.2007.03414.x.
- 707 Lobkis, O. I., and R. L. Weaver (2001), On the emergence of the Greens function in the
708 correlations of a diffuse field, *J. Acous. Soc. Am.*, 110, 3011–3017.
- 709 Moschetti, M. P., M. H. Ritzwoller, and N. M. Shapiro (2007), Ambient noise tomography
710 from the first two years of the USArray Transportable Array: Group speeds in the
711 western US, *Geochem. Geophys. Geosys.*, in review.
- 712 Ritzwoller, M., N. Shapiro, M. Barmin, and A. Levshin (2002), Global surface wave
713 diffraction tomography, *J. Geophys. Res.*, 107(B12), 2335–2348.
- 714 Ritzwoller, M. H., and A. L. Levshin (1998), Eurasian surface wave tomography - group
715 velocities, *J. Geophys. Res.*, 103(B3), 4839–4878.
- 716 Sabra, K. G., P. Gerstoft, P. Roux, W. Kuperman, and M. C. Fehler (2005), Surface
717 wave tomography from microseisms in Southern California, *Geophys. Res. Lett.*, 32(14),
718 14,311–14,311.
- 719 Shapiro, N., and M. Campillo (2004), Emergence of broadband Rayleigh waves from
720 correlations of the ambient seismic noise, *Geophys. Res. Lett.*, 31(7), 1615–1619.
- 721 Shapiro, N. M., and M. H. Ritzwoller (2002), Monte-Carlo inversion for a global shear-
722 velocity model of the crust and upper mantle, *Geophys. J. Int.*, 151(1), 88–105.

- 723 Shapiro, N. M., M. Campillo, L. Stehly, and M. H. Ritzwoller (2005), High-resolution
724 surface-wave tomography from ambient seismic noise, *Science*, 307(5715), 1615–1618.
- 725 Snieder, R. (2004), Extracting the Greens function from the correlation of coda waves: A
726 derivation based on stationary phase, *Phys. Rev. E.*, 69(4), 46,610–46,610.
- 727 Spetzler, J., J. Trampert, and R. Snieder (2002), The effect of scattering in surface wave
728 tomography, *Geophys. J. Int.*, 149(3), 755–767.
- 729 Stehly, L., M. Campillo, and N. Shapiro (2006), A study of the seismic noise from its long-
730 range correlation properties, *J. Geophys. Res.*, 111(B10), doi:10.1029/2005JB004237.
- 731 Trampert, J., and J. Woodhouse (1996), High resolution global phase velocity distribu-
732 tions, *Geophys. Res. Lett.*, 23(1), 21–24.
- 733 van der Lee, S., and G. Nolet (1997), Upper mantle S velocity structure of North America,
734 *J. Geophys. Res.*, 102(B10), 22,815–22,838.
- 735 Villasenor, A., Y. Yang, M. H. Ritzwoller, and J. Gallart (2007), Ambient noise surface
736 wave tomography of the Iberian Peninsula: Implications for shallow seismic structure,
737 *Geophys. Res. Lett.*, 34(11), doi:10.1029/2007GL030164.
- 738 Wapenaar, K. (2004), Retrieving the elastodynamic Green's function of an arbitrary in-
739 homogeneous medium by cross correlation, *Phys. Rev. Lett.*, 93(25), 254,301–254,301.
- 740 Weaver, R. L., and O. I. Lobkis (2001), Ultrasonics without a source: Thermal fluctuation
741 correlations at MHz frequencies, *Phys. Rev. Lett.*, 87(13).
- 742 Yang, Y., M. Ritzwoller, A. Levshin, and N. Shapiro (2007), Ambient noise Rayleigh wave
743 tomography across Europe, *Geophys. J. Int.*, 168(1), 259–274.
- 744 Yao, H., R. D. van der Hilst, and M. V. de Hoop (2006), Surface-wave array tomography
745 in SE Tibet from ambient seismic noise and two-station analysis-I. Phase velocity maps,

⁷⁴⁶ *Geophys. J. Int.*, 166(2), 732–744.

⁷⁴⁷ Yoshizawa, K., and B. Kennett (2002), Determination of the influence zone for surface

⁷⁴⁸ wave paths, *Geophys. J. Int.*, 149(2), 440–453.

Table 1. Number of Rayleigh wave measurements rejected and selected prior to tomography at 10-, 16-, 25-, 50-, and 70-sec periods.

| <i>Period</i> | 10-sec | 16-sec | 25-sec | 50-sec | 70-sec |
|----------------------------------|--------|--------|--------|--------|--------|
| Total waveforms | 18554 | 18554 | 18554 | 18554 | 18554 |
| Distance rejections | 421 | 864 | 1541 | 3398 | 4748 |
| <i>Group velocity rejections</i> | | | | | |
| Stdev not computed or SNR < 15 | 10385 | 7972 | 7870 | 11250 | 11560 |
| Stdev > 100 m/sec | 445 | 564 | 1148 | 1589 | 995 |
| Time residual rejection | 182 | 222 | 104 | 32 | 29 |
| Remaining group measurements | 7121 | 8932 | 7891 | 2285 | 1222 |
| <i>Phase velocity rejections</i> | | | | | |
| Stdev not computed or SNR < 15 | 10423 | 8003 | 7894 | 11275 | 11554 |
| Stdev > 100 m/sec | 355 | 676 | 1103 | 408 | 143 |
| Time residual rejection | 161 | 321 | 135 | 58 | 36 |
| Remaining phase measurements | 7194 | 8690 | 7881 | 3415 | 2073 |

Table 2. Same as Table 1 but for Love waves.

| <i>Period</i> | 10-sec | 16-sec | 25-sec |
|----------------------------------|--------|--------|--------|
| Total waveforms | 18554 | 18554 | 18554 |
| Distance rejections | 421 | 864 | 1541 |
| <i>Group velocity rejections</i> | | | |
| Stdev not computed or SNR < 15 | 9787 | 7463 | 13810 |
| Stdev > 100 m/sec | 1678 | 2211 | 1172 |
| Time residual rejection | 222 | 245 | 63 |
| Remaining group measurements | 6446 | 7771 | 1968 |
| <i>Phase velocity rejections</i> | | | |
| Stdev not computed or SNR < 15 | 9770 | 7438 | 13810 |
| Stdev > 100 m/sec | 1834 | 4005 | 1114 |
| Time residual rejection | 200 | 166 | 94 |
| Remaining phase measurements | 6329 | 6081 | 1995 |

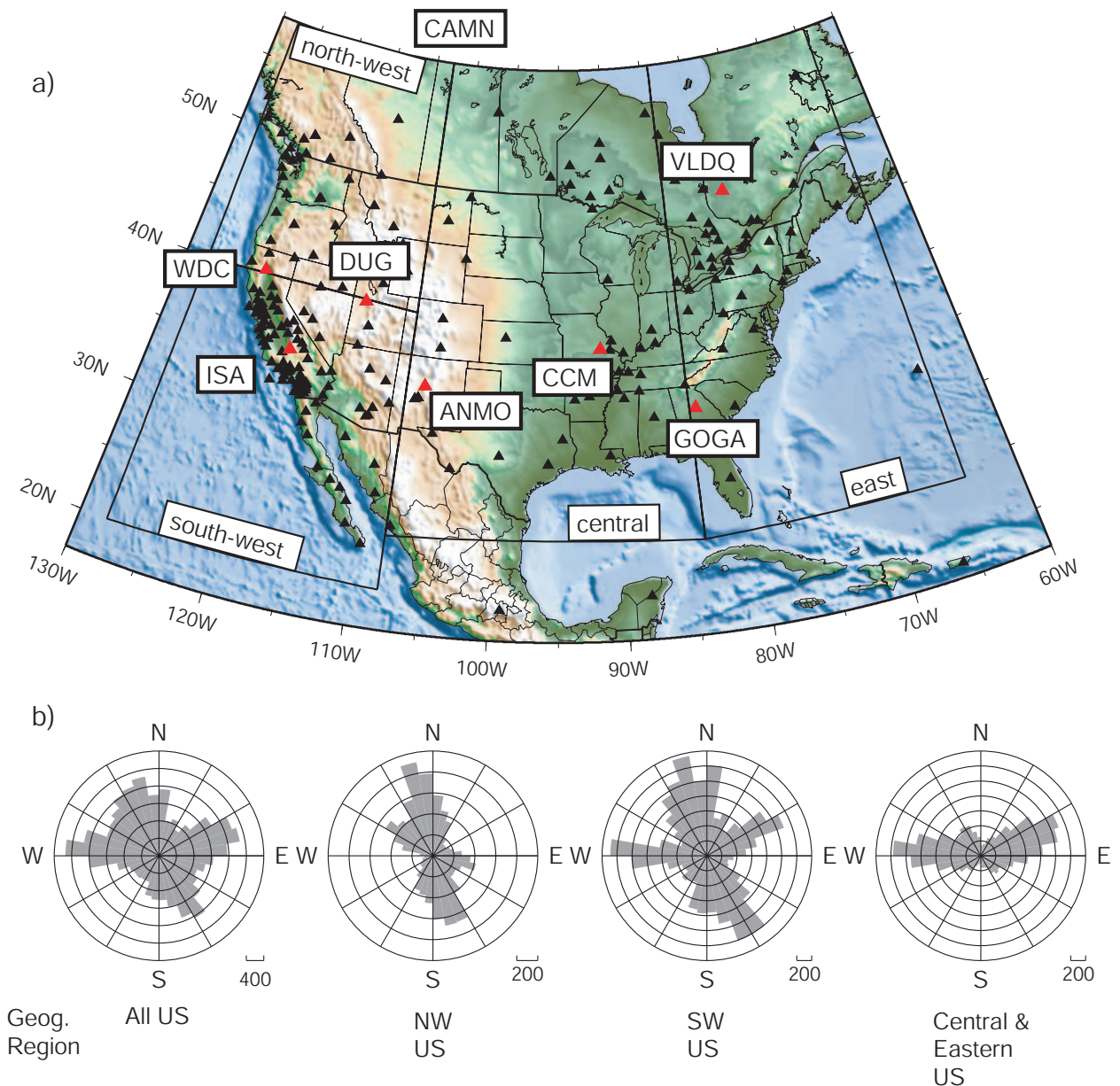


Figure 1. (a) The study area with stations represented as triangles. Red triangles with station names indicate inter-station paths for the waveforms and dispersion curves in Fig. 2. The study area is divided into four boxed sub-regions. (b) Azimuthal distribution of inter-station paths, plotted as the number of paths per 10° azimuthal bin, for the entire data set (at left) and in several sub-regions. Both azimuth and back-azimuth are included and indicate the direction of propagation of waves.

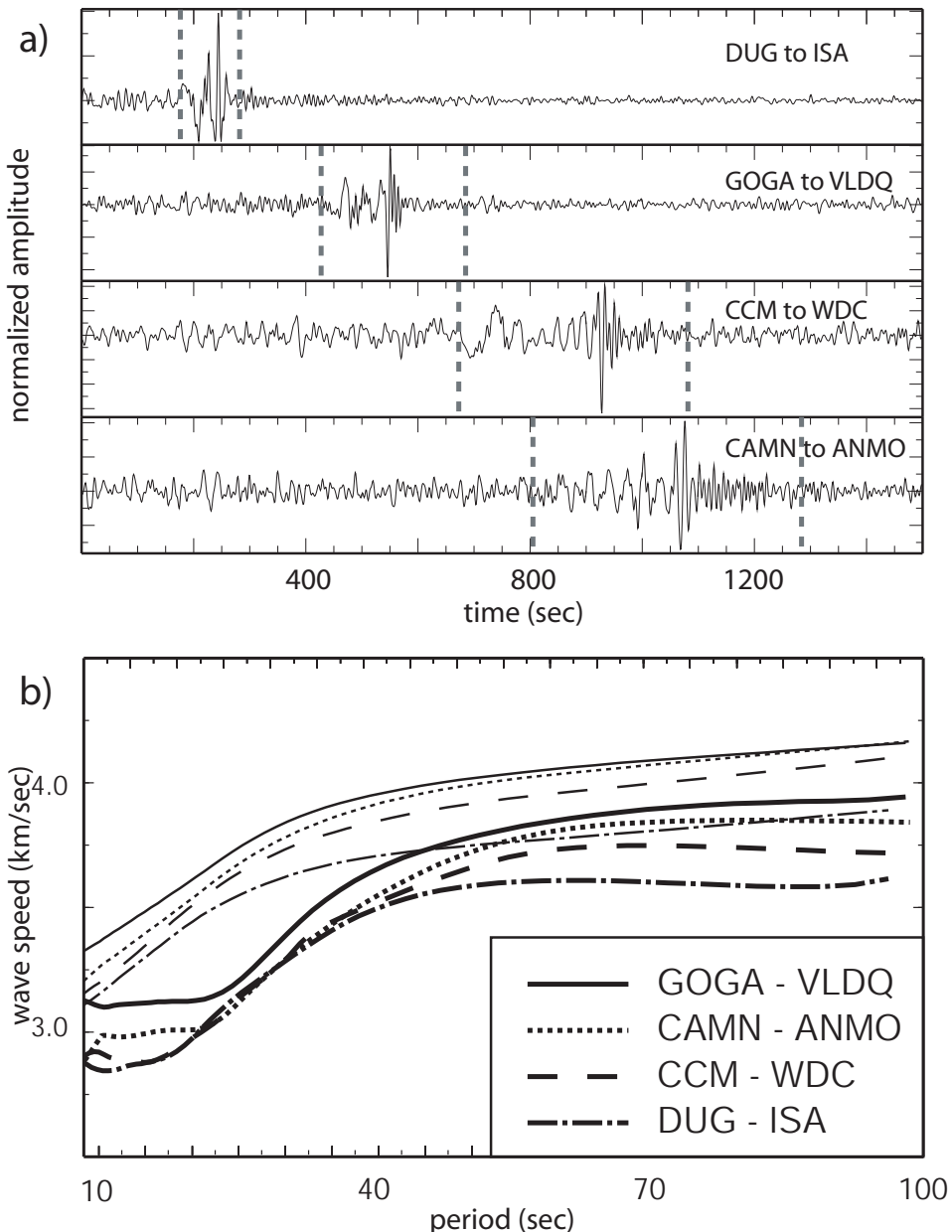


Figure 2. (a) Examples of broad-band vertical-component symmetric signal cross-correlations (Rayleigh waves) through various tectonic regimes for the inter-station paths indicated with red triangles in Fig. 1a. Waveforms are filtered between 7 and 100 seconds period. The time windows marked with vertical dashed lines are at 2.5 and 4.0 km/sec. (b) The corresponding group and phase speed curves. Group velocity curves are thicker than phase velocity curves.

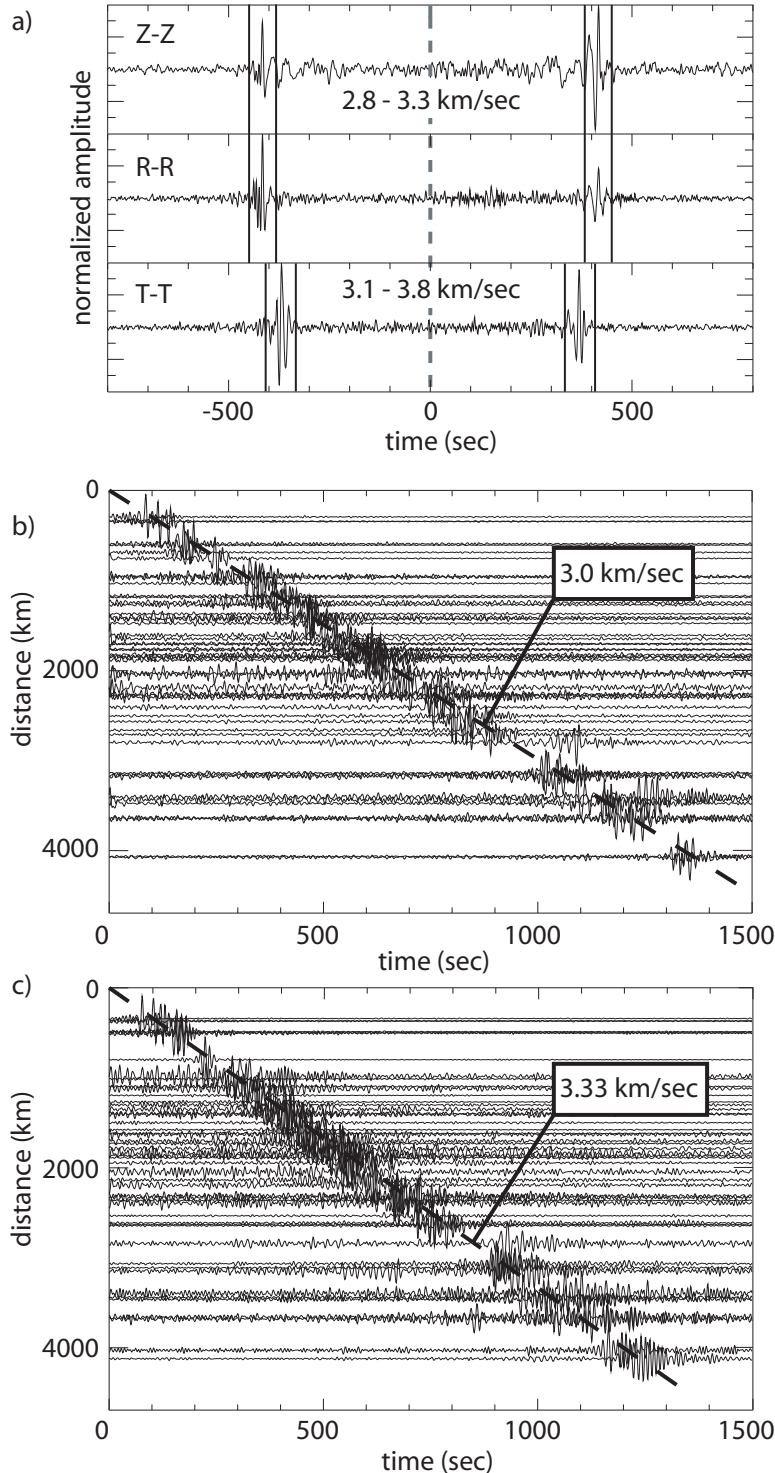


Figure 3. Example Rayleigh and Love wave empirical Green functions (EGFs). (a) Two-sided EGFs filtered between 5 and 50 seconds period for the stations CCM and RSSD. Rayleigh wave signals emerge on the Z-Z and R-R cross-correlations and are highlighted with a velocity window from 2.8 - 3.3 km/sec. Love waves are seen on the T-T component, identified with an arrival window from 3.1 - 3.8 km/sec. (b) Record section containing all D R A F T June 26, 2007, 8:41pm D R A F T cross-correlations between Z-Z components from GSN stations in the US separated by the specified inter-station distance. (c) Same as (b), but for the T-T component. Move-outs of 3.0 and 3.3 km/sec are indicated in (b) and (c), respectively.

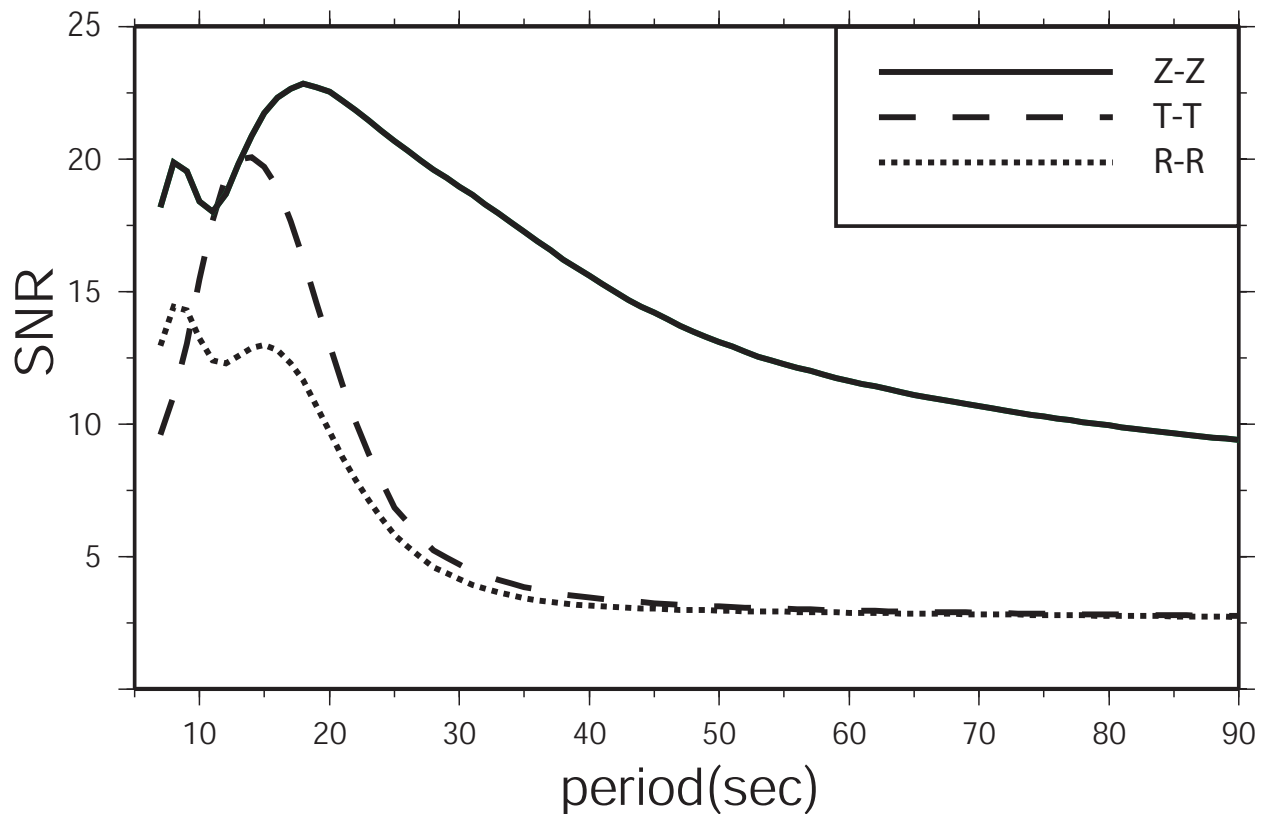


Figure 4. Relative signal quality represented as the average signal-to-noise ratio (SNR) for Rayleigh and Love waves computed using all stations in the study region. Rayleigh waves appear on vertical-vertical (Z-Z) and radial-radial (R-R) components, while Love waves are on the transverse-transverse (T-T) component cross-correlations.

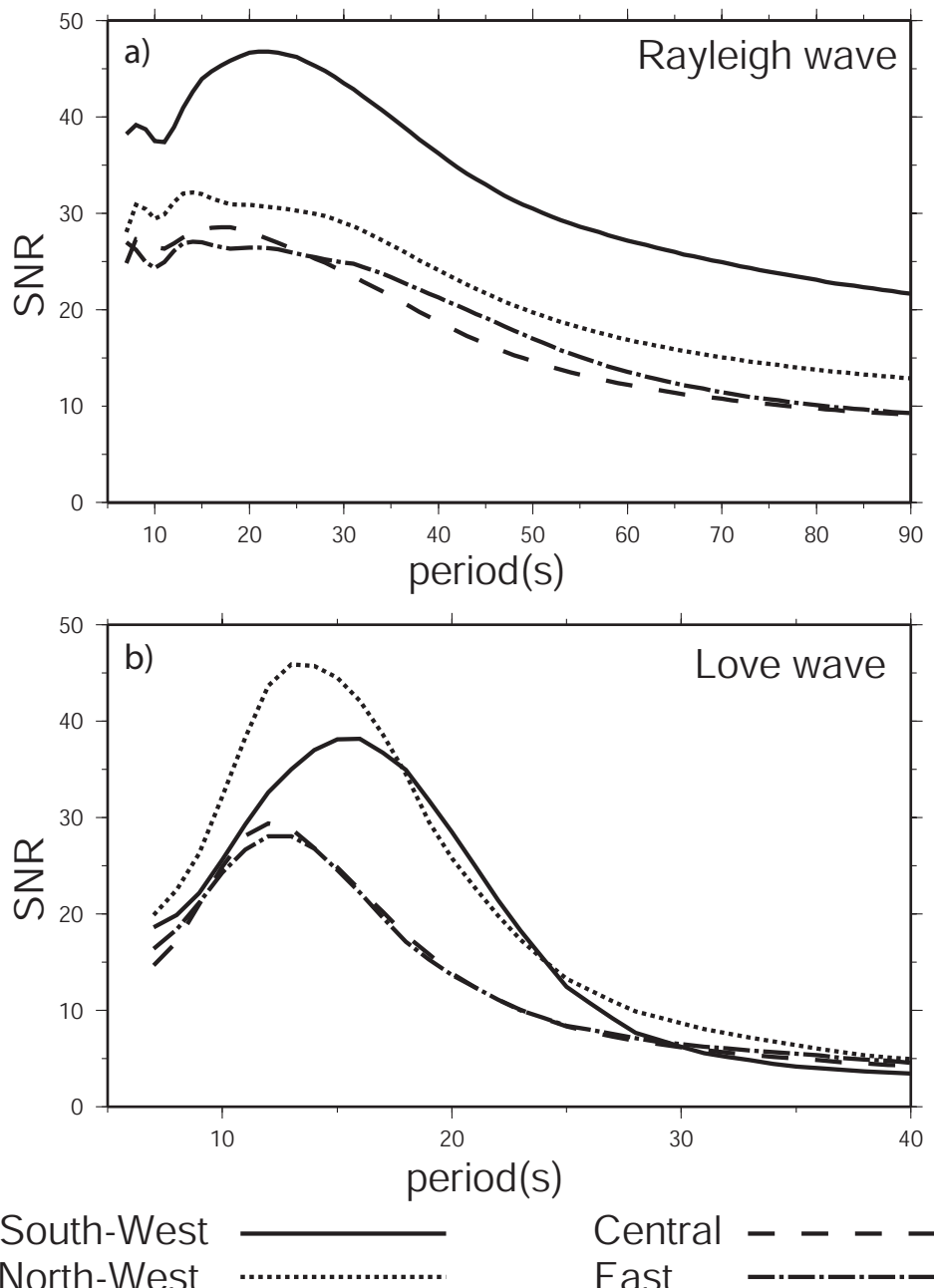


Figure 5. The mean signal-to-noise ratio is plotted versus period for (a) Rayleigh (Z-Z) waves and (b) Love (T-T) waves for the different geographical sub-regions defined in Fig. 1a. Note: the period bands for (a) and (b) differ.

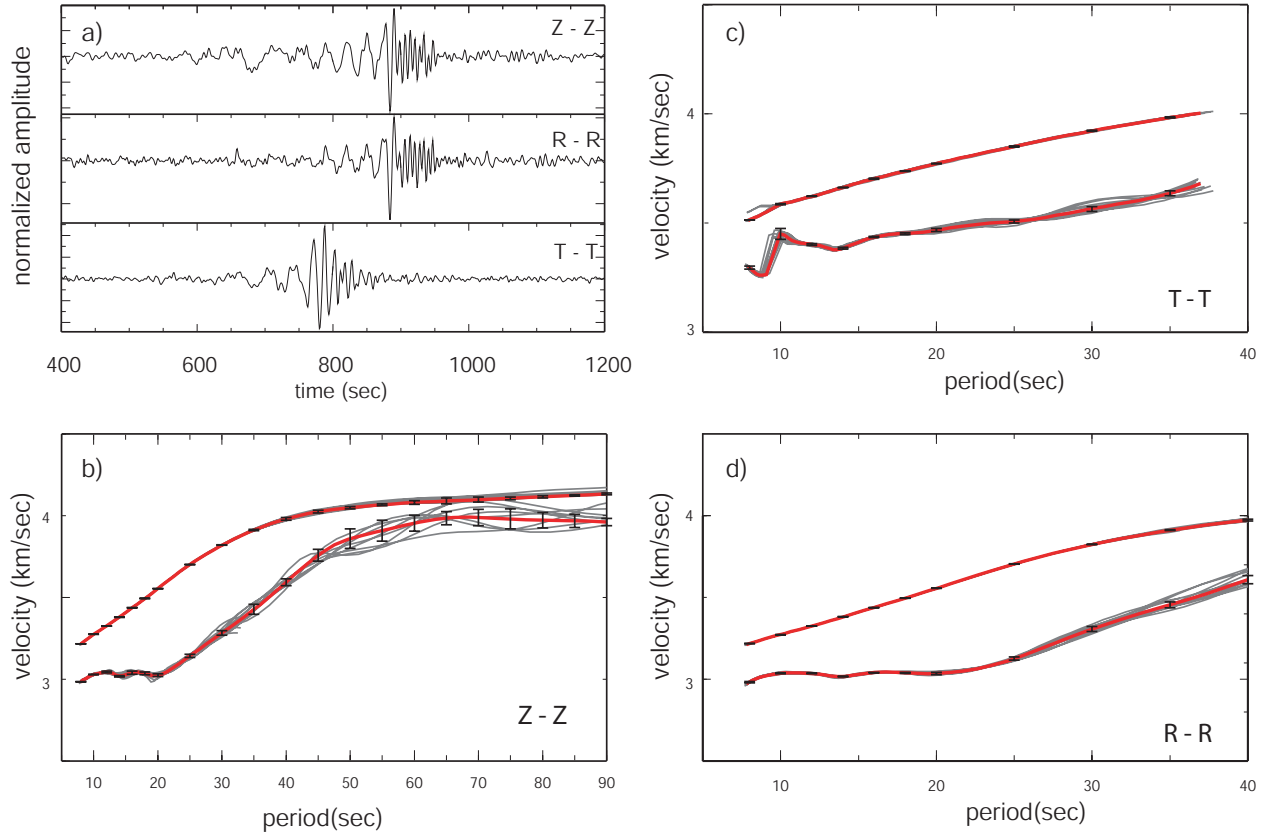


Figure 6. Illustration of the computation of measurement uncertainty. (a) Empirical Green functions on the Z-Z, R-R, and T-T components for the station pair DWPF and RSSD. (b) Measured Rayleigh wave group and phase speed curves from the Z-Z component empirical Green function. The 24-month measurements are plotted in red, individual 6-month measurements are plotted in grey, and the 1- σ error bars summarize the variation of the 6-month results. (c) Same as (b), but for the T-T component (Love waves). (d) Same as (b), but for the R-R component. Note the different period band and vertical scales in (b)-(d).

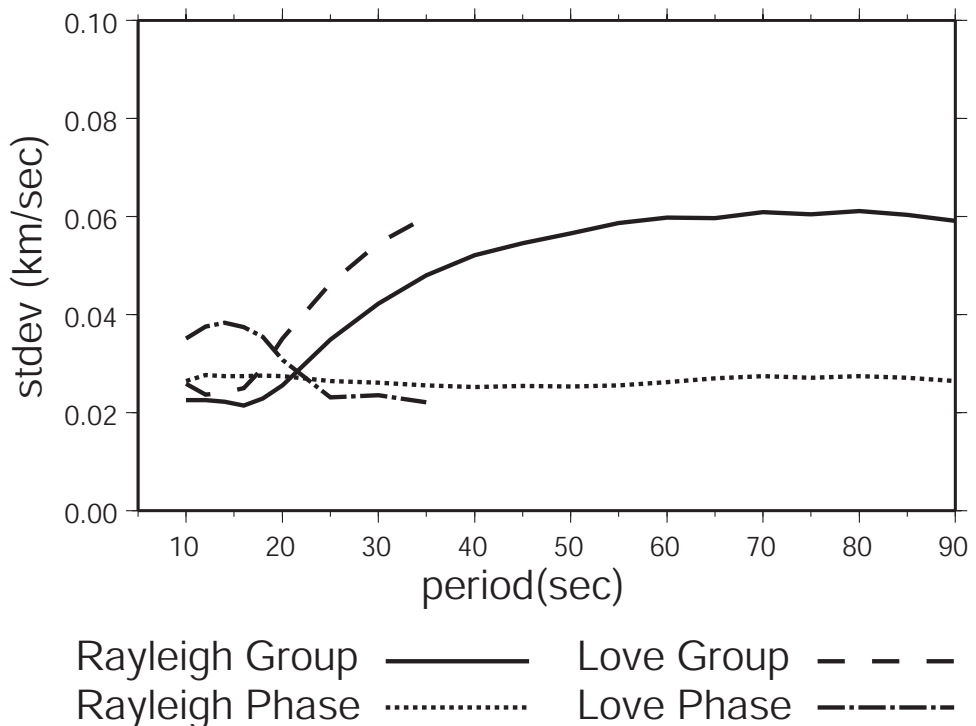


Figure 7. Average dispersion measurement standard deviation versus period for Rayleigh and Love wave group and phase speeds, where the average is taken over all acceptable measurements.

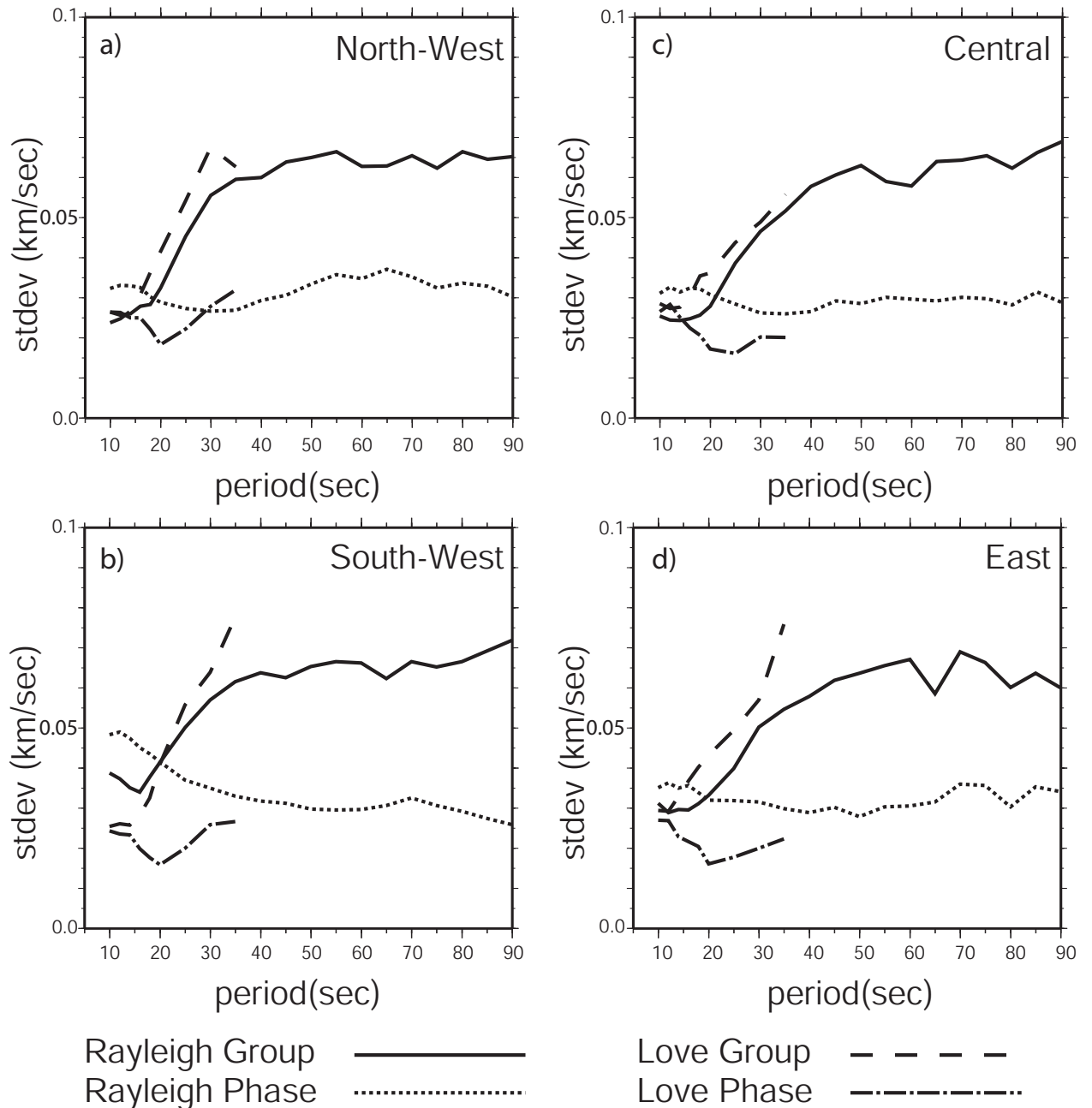


Figure 8. The average standard deviation of the velocity measurements as determined from the 6-month subsets of the data, averaged over all acceptable measurements. (a) - (d) Results are for the four sub-regions defined in Fig. 1a.

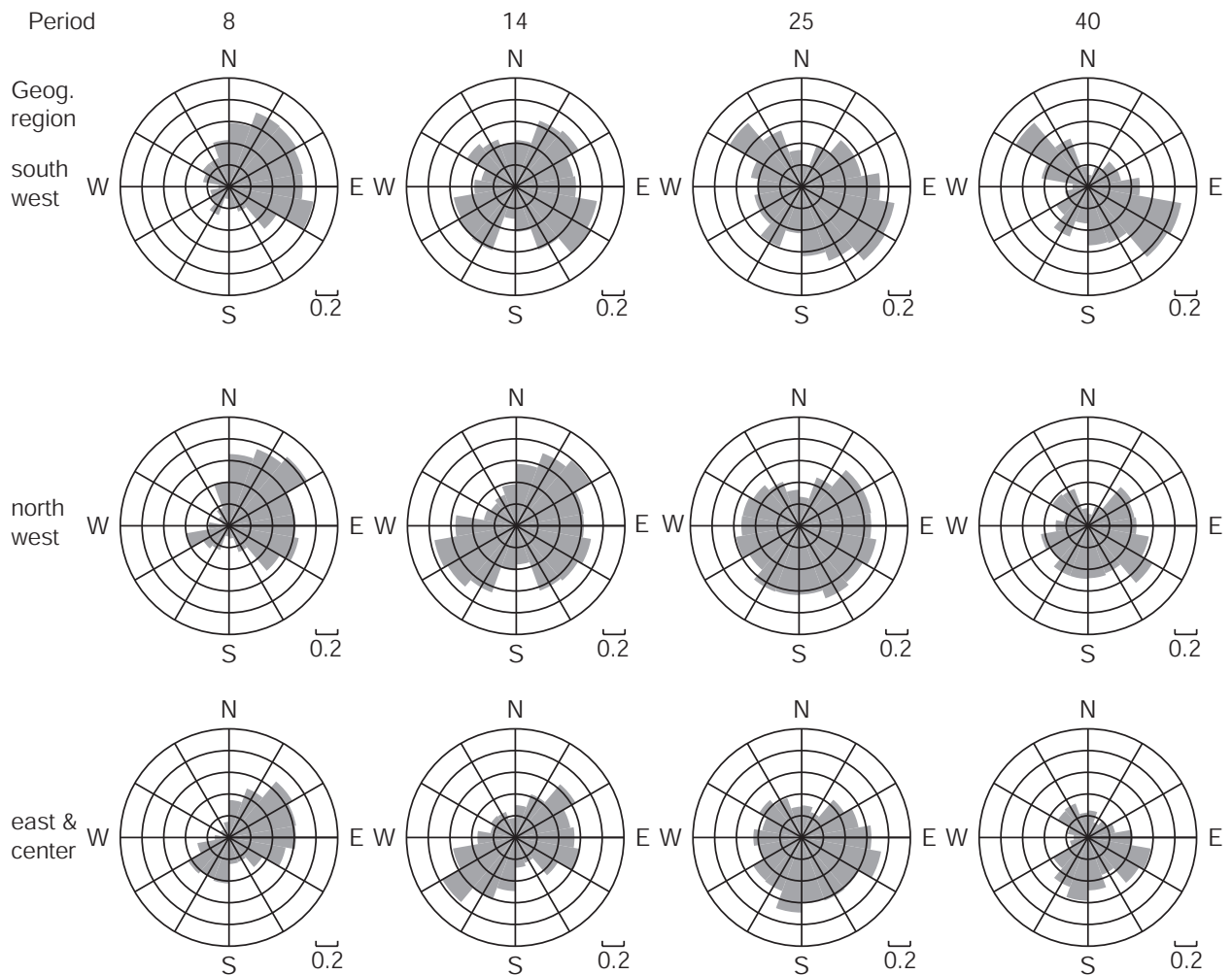


Figure 9. The directional dependence of high SNR (>10) Rayleigh wave cross-correlation signals plotted at different periods (8, 14, 25, 40 sec in different columns) and geographical sub-regions (different rows). Azimuth is the direction of propagation of the wave. Results are presented as fractions, in which the numerator is the number of inter-station paths in a particular azimuthal bin with $\text{SNR} > 10$ and the denominator is the number of paths in the bin (from Fig. 1b).

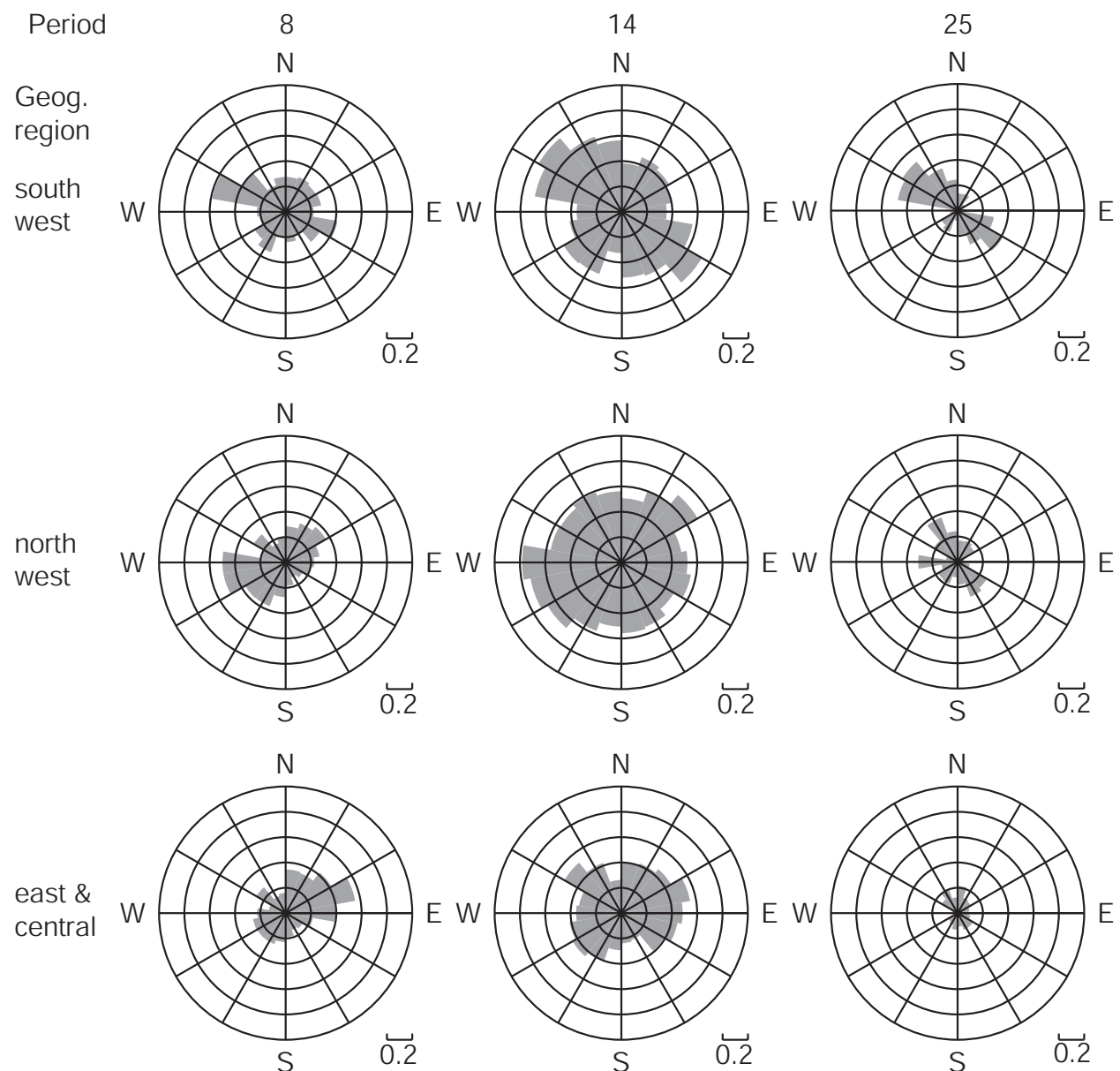


Figure 10. Same as Figure 9, but for Love waves.

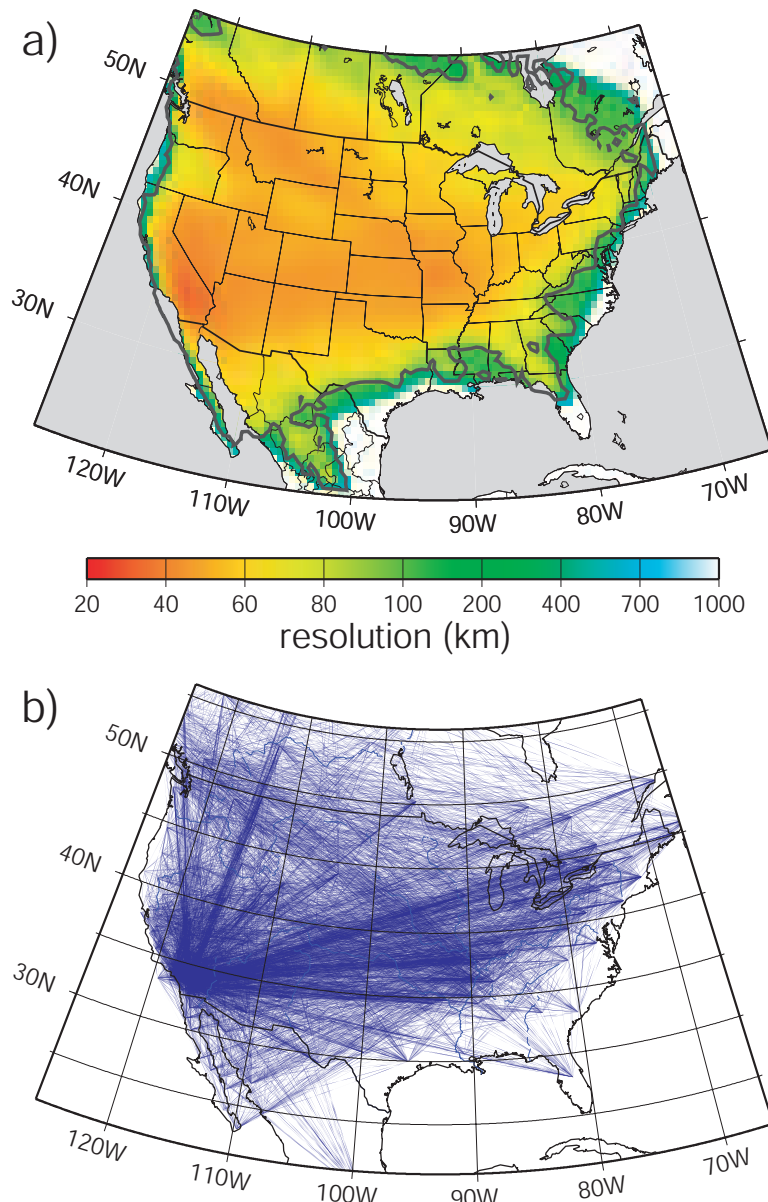


Figure 11. Path distribution and estimated resolution for the 10 sec period Rayleigh wave. (a) Resolution is defined as twice the standard deviation (2γ) of the 2-D Gaussian fit to the resolution surface at each point. The 200 km resolution contour is drawn and the color scale saturates at white when the resolution degrades to 1000 km, indicating indeterminate velocities. (b) Paths used to construct (a).

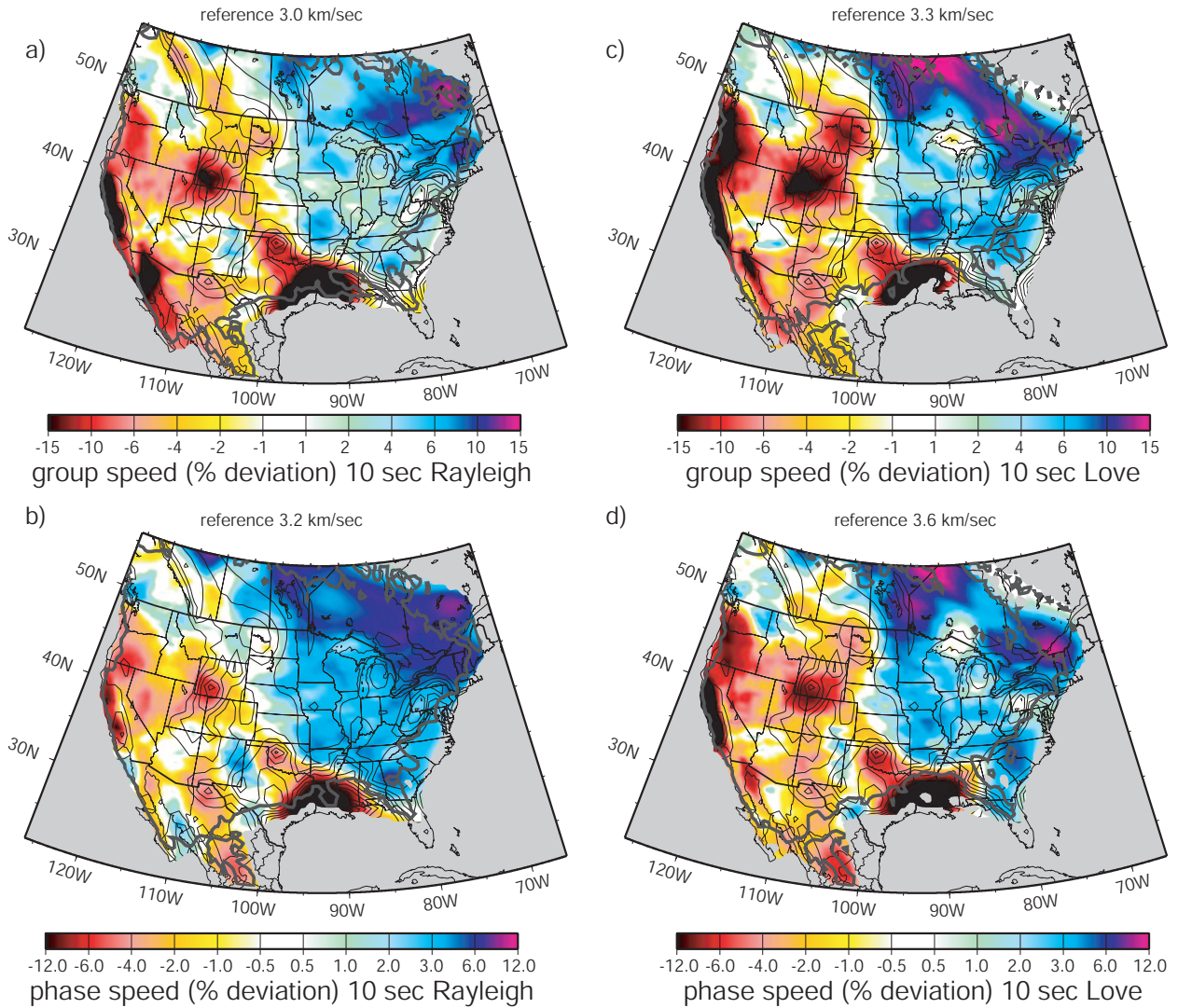


Figure 12. Rayleigh and Love wave group and phase speed dispersion maps at 10 sec period: (a) Rayleigh group speed, (b) Rayleigh phase speed, (c) Love group speed, and (d) Love phase speed. The thick grey contour outlines the region with better than 200 km resolution and areas with resolution worse than 1000 km are clipped to grey. Many sedimentary features labeled in Fig. 18 are visible and contours of the sediment model of *Laske and Masters [1997]* are plotted with thin black lines for reference. Note the differences in reference speeds and color scale ranges.

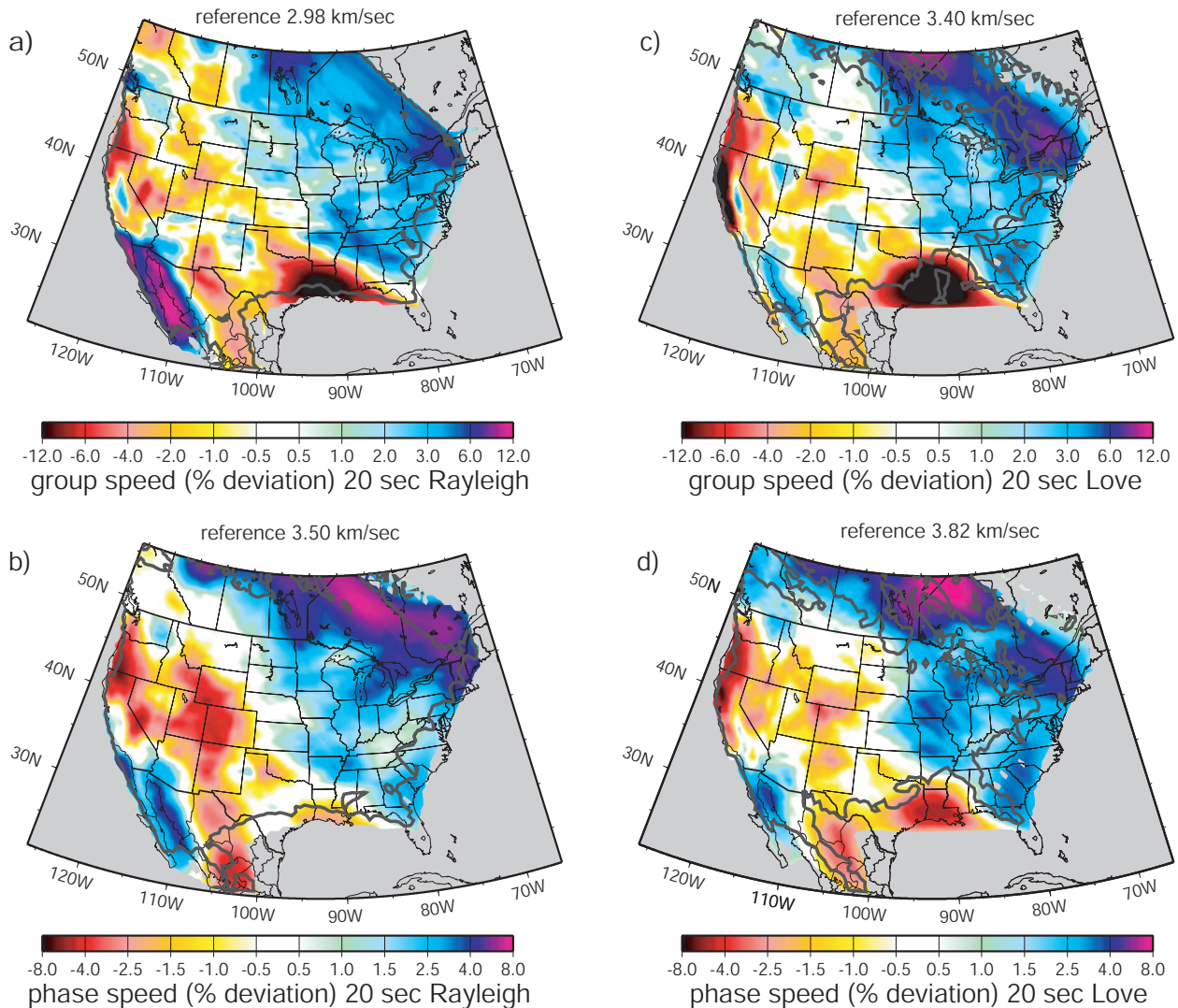


Figure 13. Same as Fig. 12, but for 20 sec period and sedimentary contours are suppressed.

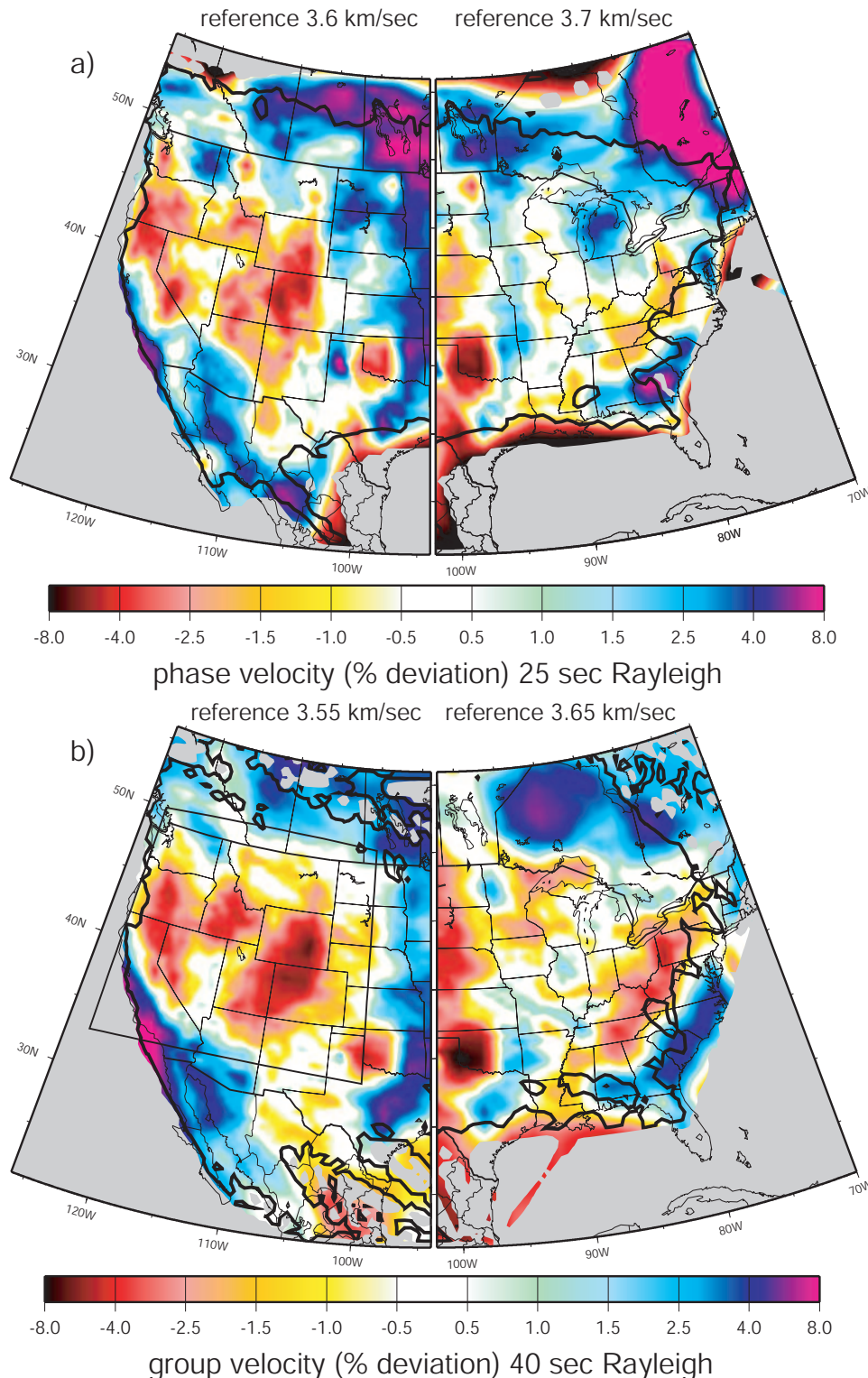


Figure 14. (a) The 25 sec period Rayleigh wave phase speed map. (b) The 40 sec Rayleigh wave group speed map. Grey contours indicate a resolution of 200 km and resolution less than 1000 km is colored grey. Different reference wave speeds are used in each half of the map and are indicated in the figure. The box in (b) corresponds to the D R A F T region blown up in Figure 19.

June 26, 2007, 8:41pm

D R A F T

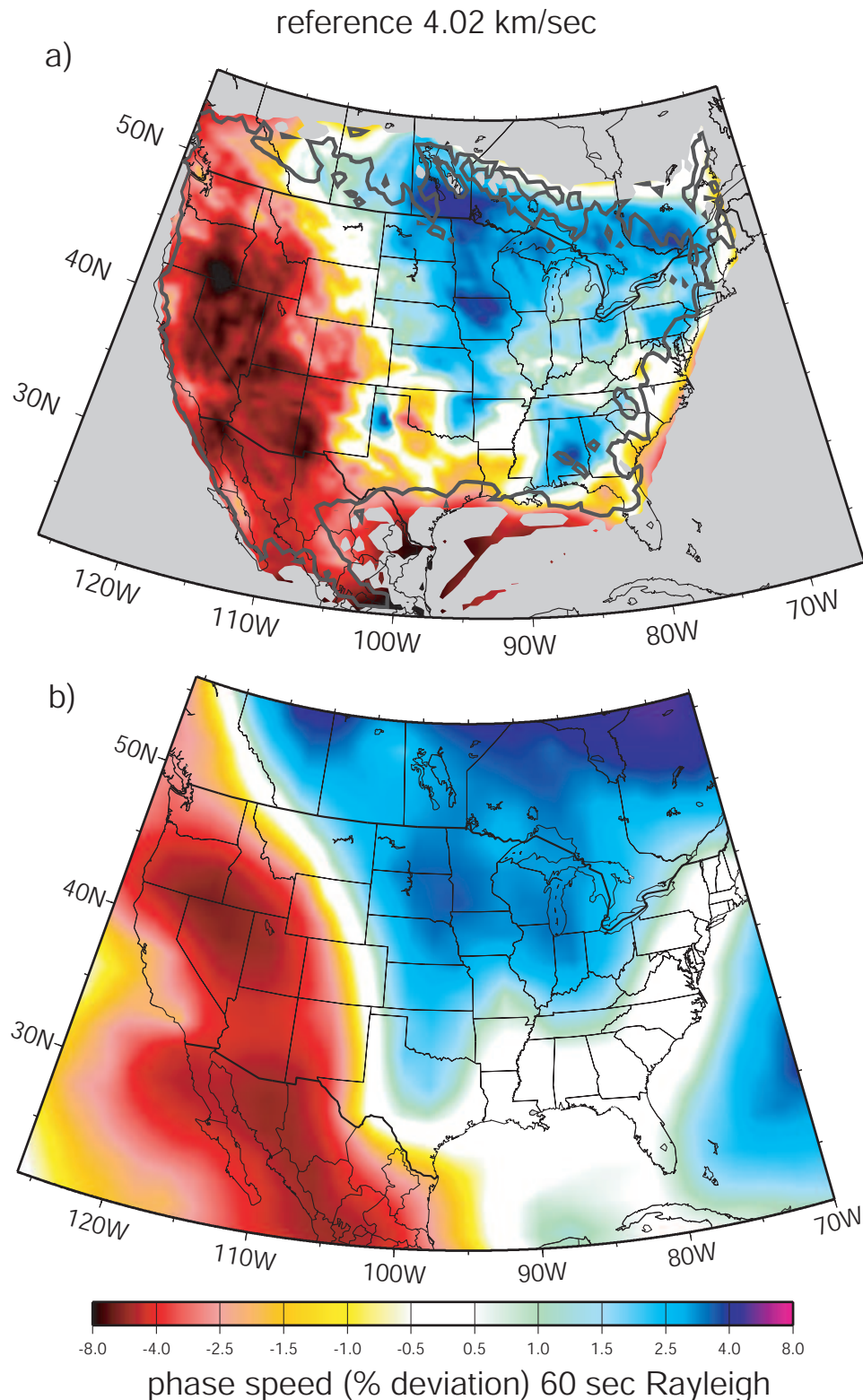


Figure 15. (a) The Rayleigh wave phase speed map at 60 sec period. The grey contour outlines the 200 km resolution and continental areas with indeterminate velocity are clipped to white. (b) The prediction from a 3-D global model (*Shapiro and Ritzwoller [2002]*) is shown for comparison.

June 26, 2007, 8:41pm

D R A F T

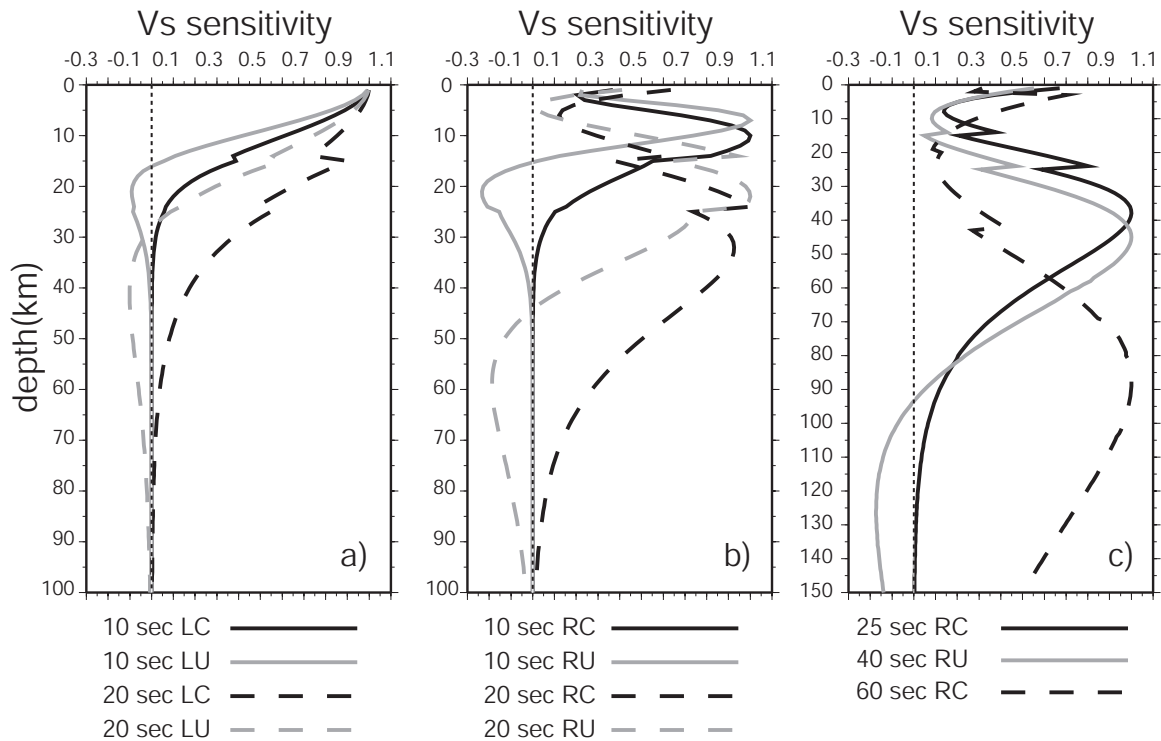


Figure 16. Sensitivity kernels for all dispersion maps shown here. The kernels have been normalized to have the same maximum amplitude and the labeling is as follows: RC - Rayleigh phase, RU - Rayleigh group, LC - Love phase, LU - Love group. Kernels are computed for PREM but with the ocean replaced by consolidated sediments.

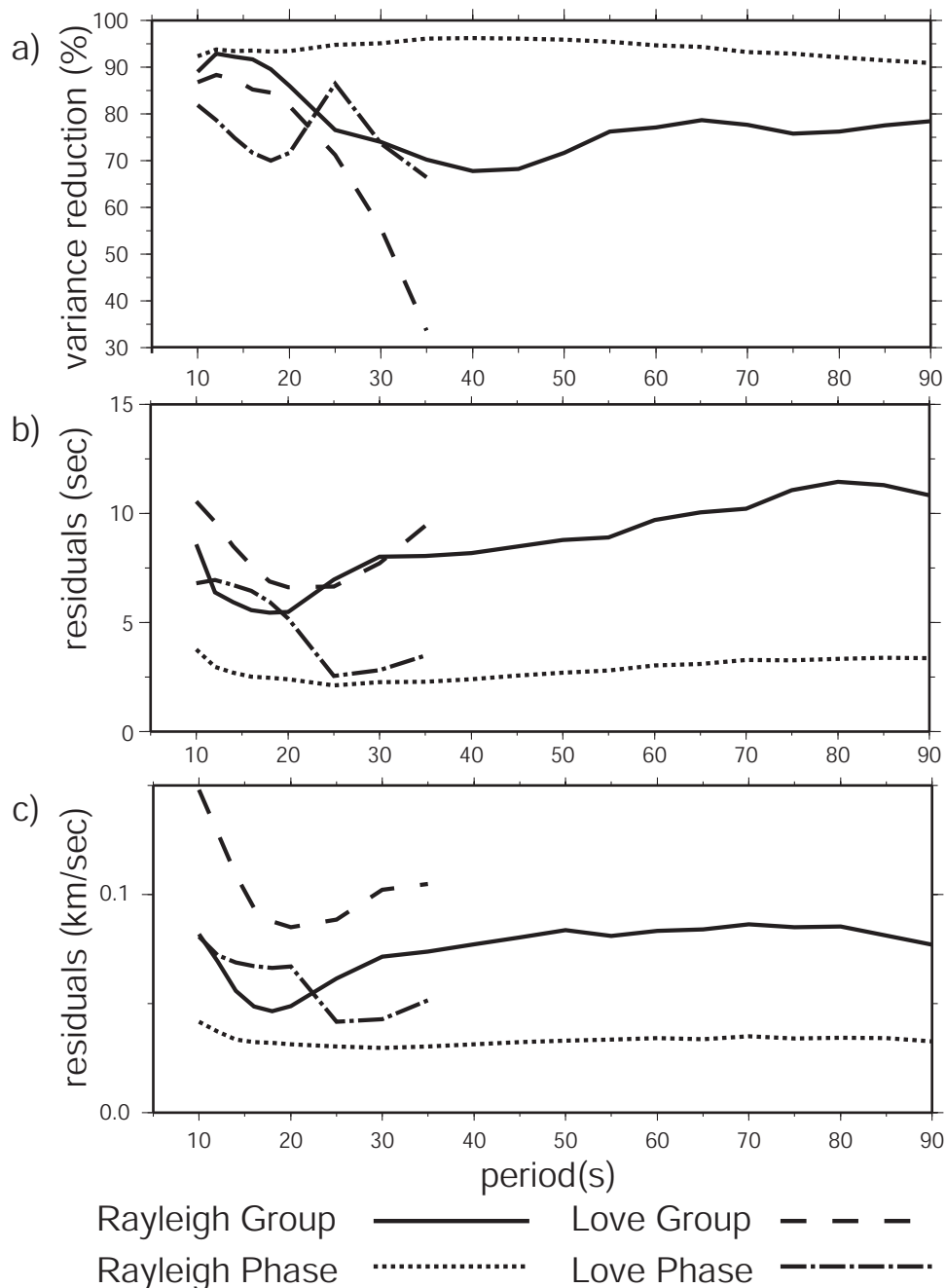


Figure 17. (a) Rayleigh and Love wave group and phase speed variance reduction as a function of period, computed relative to the mean measurement for each wave type and period. (b) The final travel-time residuals in seconds. (c) Final velocity residuals.

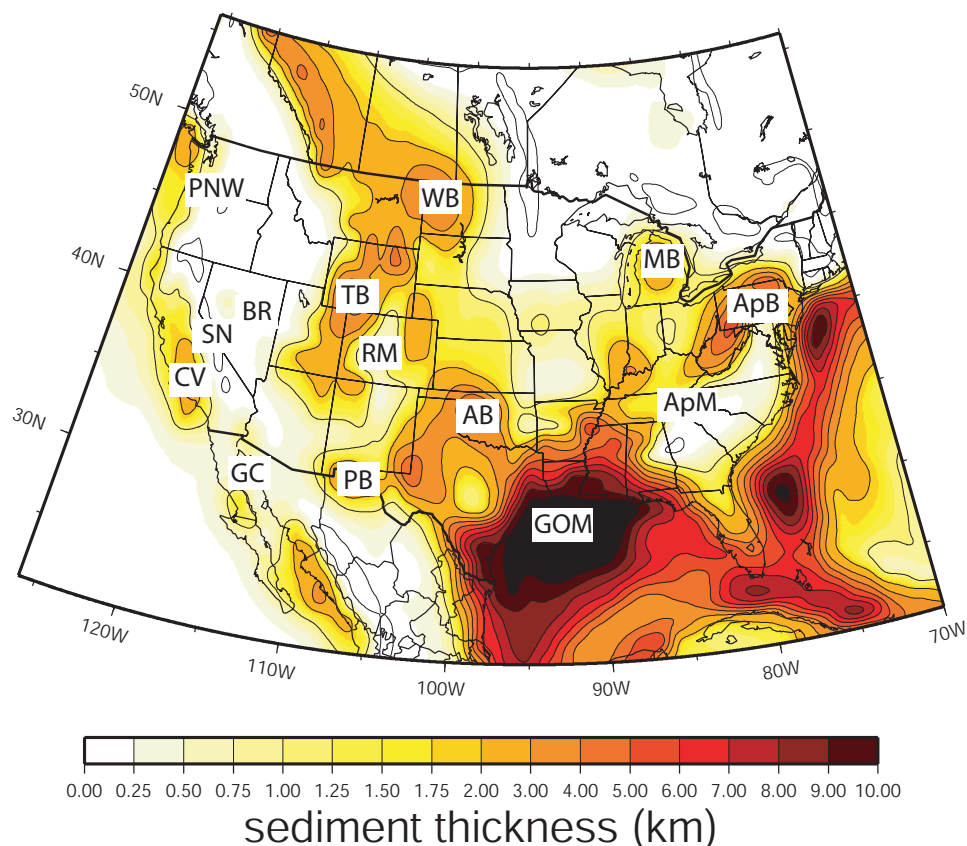


Figure 18. Sediment thickness model of *Laske and Masters* [1997] with several prominent basins and geographical features labeled: ‘CV’ - Central Valley in California, ‘SN’ - Sierra Nevada, ‘AB’ - Anadarko Basin, ‘PB’ - Permian Basin, ‘GOM’ - Gulf of Mexico, ‘TB’ - Wyoming-Utah-Idaho thrust belt, ‘WB’ - Williston Basin, ‘ApB’ - Appalachian Basin, ‘MB’ - Michigan Basin, ‘BR’ - Basin and Range, ‘RM’ - Rocky Mountain Region, ‘ApM’ - Appalachian Mountains’, ‘PNW’ - Pacific Northwest, ‘GC’ - Gulf of California.

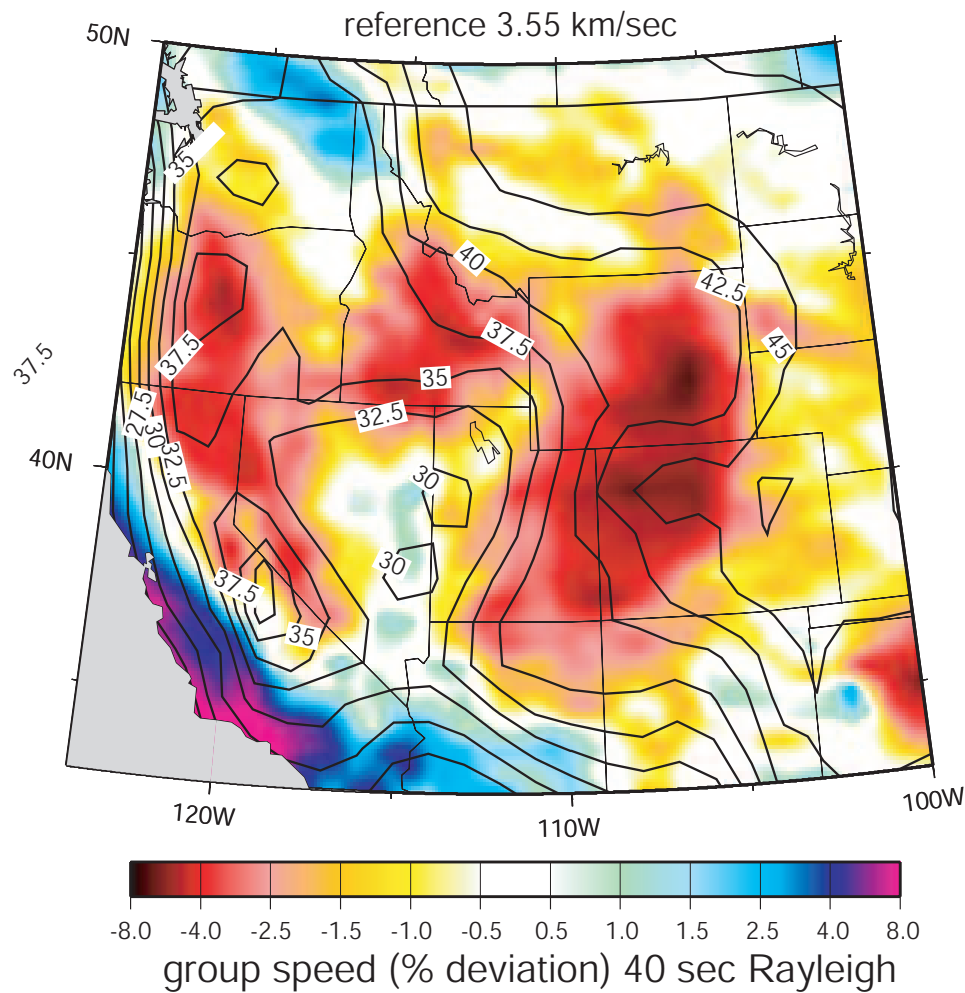


Figure 19. Rayleigh wave group speed dispersion map at 40 sec period for the region outlined in Fig. 14b. The Cornell US Moho depth model (http://discoverourearth.org/geoid/metadata/htmls/image_grid/us_moho_eq.html) is plotted as contours with a 2.5 km contour interval with a maximum thickness under Colorado of 47 km. Low velocities generally correspond to thick crust.